Growth and Characterization of $LaCrO_3$ Heterostructures

Annabella Drewanowski

Master Thesis

Supervised by

Simon Jöhr
Prof. Dr. Marta Gibert
Prof. Dr. Johan Chang

Universität Zürich[UZH]

Faculty of Science
University of Zurich
Switzerland

Contents

Abstract

This Master thesis aims to fabricate and characterize epitaxial $LaCrO_3$ (LCO) thin films on various perovskite substrates under both compressive and tensile strain. This is a crucial step towards the later goal of growing high-quality LCO/$SrCrO_3$ (SCO) perovskite superlattices via off-axis RF magnetron sputtering, with the goal of achieving exchange bias by coupling the weakly ferromagnetic LCO with the metallic and supposedly antiferromagnetic SCO at the interface. Structural characterizations, including symmetrical $\vartheta/2\vartheta$ x-ray diffraction (XRD) scans and atomic force (AFM) imaging, confirm the high crystalline quality of the LCO films. X-ray absorption spectroscopy (XAS) and X-ray magnetic circular dichroism (XMCD) reveal the chromium ion's desired oxidation state and magnetization behaviour, respectively. Superconducting quantum interference device (SQUID) magnetometry was used to study the films' magnetic properties, which revealed unexpectedly strong signals in the thick films grown for this purpose. Although some preliminary results have been achieved regarding the LCO/SCO superlattices, further work is required to improve the quality of the interfaces. Nonetheless, this work provides a detailed investigation of LCO heterostructures grown in the extremely reducing environment required to stabilize the SCO perovskite structure. It lays essential groundwork for future research in this field.

Declaration

I declare that this thesis is my own original work and has not been submitted for any degree or examination at any other university.

All sources of information and material used in the research and writing of this thesis have been duly acknowledged, including direct and indirect quotations.

I further declare that this thesis is written in accordance with the rules and regulations of the institution and that it does not infringe upon the rights of any third party.

Acknowledgements

First and foremost, I want to thank Simon Jöhr, the PhD student remaining at the UZH, who introduced me to all the lab equipment and who was my contact person throughout the several months in which the practical lab work for this thesis was done and who worked tirelessly during our all-nighter at the Paul Scherrer Institute. Thank you Dr. Cinthia Piamonteze for offering us this night to take measurements at Xtreme in SLS. I would also like to thank the other PhD student, Jonathan Spring, who was available to discuss our beamtime data. I have had great experiences and opportunities at beamlines like the low-energy muon beamline for Simon's SCO samples and the swiss light source (SLS) for Jonathan's double perovskite heterostructures and my LCO samples but also at the Diamond light source in Didcot (GB) thanks to Prof. Johan Chang, who gave me the opportunity to conduct measurements on La_2NiO_4 thin films with his team at the l21 RIXS beamline. For that, I am very grateful. I want to give special thanks to Prof. Marta Gibert for our extensive exchange during the writing process and her inspiring supervision throughout my whole time in the lab, which have helped me immensely.

Chapter 1

Introduction

Transition metal oxides (TMO) are a widely studied class of materials exhibiting an abundant variety of electronic properties which make them useful for various technological applications. Research in the last decades has led to the discovery of exotic phenomena such as high-temperature superconductivity, colossal magnetoresistance, and metal-to-insulator transitions as well as the increase in piezo/ferro and dielectric and multiferroic performances. This continues to attract interest in different fields and poses promising new candidates for diverse applications and possibly the inevitable replacement of silicon for communication technologies, micro actuation, microsensing and energy conversion [1]. The improvements in manufacturing techniques for high-quality oxide heterostructures have enabled the study and engineering of multifunctional artificial structures [2]. The wealth of properties arises from the complex interplay between electron, spin, orbit and lattice degree of freedom and structural variety of TMO, which exist in different crystal structures and compositions.

We are specifically interested in a broad subgroup of TMOs that crystallize in the perovskite structure. The transition metal cation is closely packed inside the oxygen octahedron. Complex interdependencies arise between the strongly correlated d-electrons of the transition metal and the oxygen p-orbitals [3]. The electron count on the transition metal cation is determined by the oxidation state of the rare-earth or alkaline earth cation also present in the structure. The competing energies driving the electronic behaviour are subtle and heavily influenced by the structural properties of the crystal. Hence, precise control of meta-stable phases is possible by manufacturing techniques with atomic precision and opens up new avenues for the explorations of emergent phenomena and the development of new devices on the nano-, micro- and macro scale [2].

This master project is part of a larger study on strontium chromate $SrCrO_3$ (SCO), with properties that have long been debated. Namely, the simultaneous and rare occurrence of antiferromagnetic ordering and metallic transport behaviour in its ground state. Metallic antiferromagnets have gained interest for their possible use in spintronic devices and the fundamental understanding of antiferromagnets [4]. SCO material has been synthesized as a thin film in our group, and it has been shown that if grown on a substrate that applies compressive strain, it is metallic. So, the antiferromagnetic ordering in those films remains to be shown. Antiferromagnetism in thin films is notoriously challenging to probe, since conventional methods used for bulk materials lack the sensitivity needed for small volumes such as thin films [5, 6].

We turn to another perovskite: lanthanum chromate $LaCrO_3$ (LCO), the focal point of this thesis. LCO has been studied for several decades now as it possesses high melting points, displays high conductivity if doped and high stability in oxidizing as well as reducing environments making it a promising candidate for heating elements in muffle furnaces, current-conducting electrodes in magneto-hydrodynamics and interconnectors of solid oxide fuel cells [7].

LCO is structurally compatible with SCO and it is weakly ferromagnetic due to canted antiferromagnetically ordered spins. By creating interfaces between these two weakly ferro- and antiferromagnetic materials an exchange anisotropy is induced. The supposed antiferromagnetic

ordering of SCO can then be indirectly verified through the exchange bias phenomenon in magnetization measurements.

The goal of this thesis was the growth of LCO via sputtering deposition and conducting a thorough structural as well as electronic characterization. Ultimately, high-quality synthesis is needed for the fabrication of the aforementioned artificially layered heterostructures containing LCO and SCO layers creating atomically controlled interfaces between the two for the magnetization measurements.

Chapter 2 discusses concepts related to the crystal structure and interconnection between crystal symmetry, electronic properties and strain, briefly touched upon at the beginning of this introduction. A more detailed introduction to LCO can be found in **Section 2.5**. LCO was indeed successfully grown and thoroughly characterized. Its structural and electronic properties were characterized by the use of various instruments and methods explained in **Chapter 3**. The characterization is summarized and discussed in **Chapter 4** including some documentation on the first attempts at the layered LCO/SCO heterostructure presented as preliminary results.

Chapter 2

Perovskite Heterostructures

In the ideal case, the perovskite structure has a cubic unit cell belonging to the space group $Pm\bar{3}m$ with the chemical formula ABO_3. The A-cation is located at each corner of the cube, the B-cation is located in the middle and it is six-fold coordinated by the face-centred oxygen forming an octahedron (**fig. 2.1**).

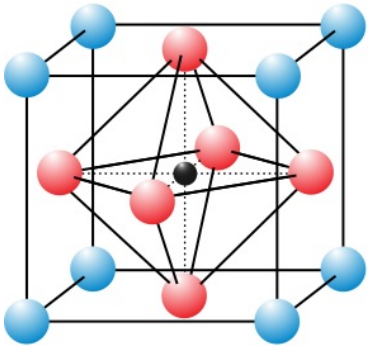

Figure 2.1: ABO_3 perovskite structure.

2.1 Crystal Structure and Symmetry breaking

For many perovskites, crystal symmetry may be reduced due to distortions. The Goldschmidt tolerance factor t determines the degree of distortions [8]. It is found by simple geometric considerations, where the atoms are balls packed into the cube. The B-cation must fit inside the oxygen octahedron while the A-cation and the oxygen must fit in the diagonal of the cube. This is expressed as

$$a = 2(r_O + r_B) \tag{2.1}$$

$$a = \frac{2}{\sqrt{2}}(r_O + r_A) \tag{2.2}$$

where r is the ionic radii of the atoms in the perovskite crystal and a is the lattice parameter i.e. the side of the cube. The tolerance factor is determined by dividing 2.1 by 2.2

$$t = \frac{r_O + r_A}{\sqrt{2}(r_O + r_B)} \tag{2.3}$$

For $t = 1$ the atoms can be packed nicely into a cube. However, distortions occur by varying the relative sizes of the atoms. If the radius r_B is increased ($t \leq 1$) the B-cation is too large to fit and the oxygen octahedron will deform itself in order to accommodate the B-atom. If r_B is decreased ($t \geq 1$) the B-cation can move within its oxygen cage and displace itself from the centre

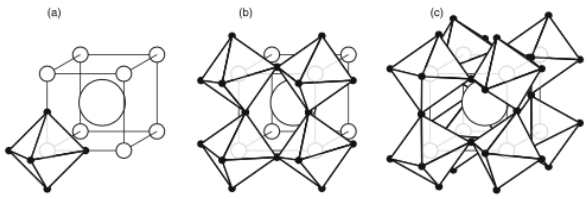

Figure 2.2: a) cubic perovskite, b) tetragonal distortion ($a^0a^0c^-$) with one out-of-phase tilt along the c-axis and c) orthorhombic distortion with a more complicated tilting system. Comparing to the tetagonal case, the tilts also cause out-of-phase distortions in the in-page direction. Image credits [9]

of the cube breaking inversion symmetry and allowing for a B-driven ferroelectric behaviour, as observed in materials such as lead titanate ($PbTiO_3$) and barium titanate ($BaTiO_3$). This displacement can either be polar for which the repetition of the microscopic dipolar unit cell will lead to a net polarization or antipolar where the displacement alternates in two directions leading to a net zero polarization. Any of these deformations will lead to changes in bond length and bond angles between the B-atom and oxygen. Typically, in the tolerance range $0.9 < t < 1$ the cubic structure is stable. For $t < 0.9$ the cubic structure is no longer stable and the system falters to an orthorhombic (Pbnm) (see **fig. 2.2**) or rhombohedral (R3c) structure [9].

The accommodations in the form of octahedral rotations were classified by A.M. Glazer, of which there are 15 unique ways to rigidly distort the octahedron [10]. The distortion in the Glazer notation is described by a string of three letters and for each there is a superscript value of $+$ or $-$ or 0. The letters denote the magnitude of a tilt along the crystallographic axes and the superscript denotes whether the tilts are in phase $+$ or out of phase $-$ along the respective axis or if there is a lack of a tilt 0. For example, a tilt that repeats every second cubic unit cell in direction (001) leads to a tetragonal unit cell denoted by $a^0c^0c^-$.

A pseudocubic unit cell can be introduced for crystal systems that exhibit structural distortions. Although the conventional unit cell is not cubic, a cubic-like unit can be isolated by making some approximations using the information of the conventional unit cell. This artificial construction is used to quantitatively compare different perovskite crystals with each other. An example of such a construction for an orthorhombic distortion is shown in **figure 2.8**.

2.2 Heterostructures

Heterostructures are artificial layered systems consisting of different compositions engineered with a high degree of control in the nanoscale range. The purpose is to study emergent phenomena created at interfaces of these layers [3] or to design functional devices [1].

A ***thin film*** is composed of a substrate (thickness $\leq 1\,\text{mm}$) that imposes a crystalline order and lattice strain on to the layers deposited on top (up to tens of nanometers). The atoms of the film bond to the substrate and adopt the in-plane lattice parameters leading to distortion of the film's bulk unit cell. If the layers have a single crystalline order, the thin film is considered epitaxial. Because of the strong interplay between electronic properties and crystal structure, lattice strain can tune certain properties or stabilize certain phases.

A ***superlattice*** consists of layers of different crystalline compounds. The smallest repeating unit, consisting of layers with thicknesses n, m, is repeated x-times throughout the structure denoted as $(n, m)x$. For example, interface effects can be studied with such structures by creating superlattices of the same total thickness and measuring certain properties as a function of the number of interfaces.

The ***exchange bias*** is an example of an interface-driven technological relevant phenomenon that occurs for instance at the interface between a ferromagnetic and an antiferromagnetic layer. The spins at the interface are exchange coupled, which contributes an exchange anisotropy to the total magnetic energy of the ferromagnetic film [6]. The antiferromagnetic layer is a fixed layer

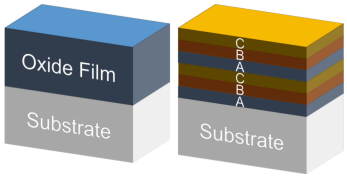

Figure 2.3: A schematic picture of an oxide thin film (left) and an oxide superlattice (right) grown on a substrate. The thin film will be grown on different substrates to study the effect of the strain. To investigate the effect of thickness, the thin film is grown for different sputtering times. This superlattice consists of three different layers A, B and C with a periodicity of $x = 2$.

with respect to externally applied fields, while the ferromagnetic layer is switchable. Exchange bias in magnetization versus field loops results in the pinned ferromagnetic spins switching at higher fields during the positive-to-negative and negative-to-positive field sweeps. The exchange bias manifests itself in a shift along the H-axis of the hysteresis curve of such heterostructures (see **fig. 2.4**). This is why this method can be used to indirectly verify antiferromagnetic ordering, provided one of the layers is a known ferromagnet.

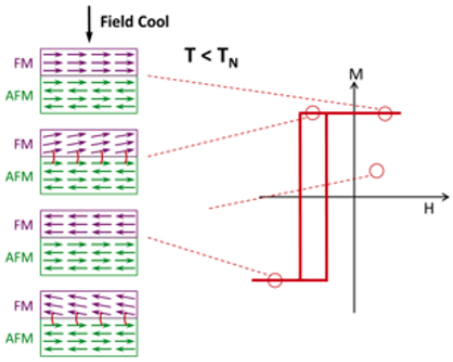

Figure 2.4: This is a diagram of the exchange bias in which one can see how the M(H) curve is shifted on the axis of the applied field. At temperatures below the Néel temperature, the spins at the FM/AFM interface will be either aligned or anti-aligned. Thus there is an anisotropy in the coupling. In the diagram, the spins of the FM are aligned with the magnetic field when cooled in the field. By decreasing the field to negative values the spin orientation of the ferromagnetic layer will eventually switch. The switching from parallel alignment to anti-parallel alignment requires stronger fields than the other way around due to the exchange interaction.

2.3 Strain

The substrate applies strain on the thin film, either by compression or tension, leading to distortions of the bulk's unit cell, changing its dimensions and symmetry. Tensile strain is applied when the in-plane lattice parameters of the substrate are larger compared to the bulk lattice parameters of the film, and compressive strain is applied when the opposite is true. Strain ϵ refers to the deformation or distortion of a material, which is measured by the change in length Δl_i divided by the original length l_i in a given direction i. This change is typically caused by stress σ, which is defined as the amount of force applied per unit area. Both variables are related by Young's modulus, a material constant valid for elastic deformation

$$\sigma = Y\epsilon$$

Consider an isotropic thin film with dimensions of $l \times d \times t$ (**see fig. 2.5**). According to Hooke's law, applying a force normal to the $d \times t$ surface will cause deformation in all three dimensions.

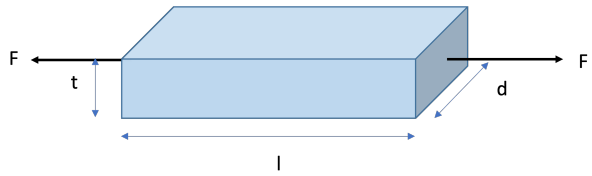

Figure 2.5: A thin film with dimensions $l \times d \times t$ and tensile strain applied along the $t \times d$ normal.

Specifically, the changes along d and t will be related to the change in length l by a factor of the material's Poisson's ratio ν, which is usually greater than zero and less than 0.5 for all materials. This can be expressed mathematically as $\Delta d/d = \Delta t/t = -\nu \Delta l/l$ with an opposing sign. It follows from the considerations above, that strain along one dimension is due to stress along that same dimension or stress applied along the other two directions with consideration of Poisson's ratio:

$$\epsilon_x = \frac{1}{Y}[\sigma_x - \nu(\sigma_y + \sigma_z)]$$
$$\epsilon_y = \frac{1}{Y}[\sigma_y - \nu(\sigma_x + \sigma_z)]$$
$$\epsilon_z = \frac{1}{Y}[\sigma_z - \nu(\sigma_y + \sigma_x)]$$

To simplify the equations above for an isotropic material experiencing biaxial stress in the in-plane directions (x and y), we can set σ_z to 0, as is the case for epitaxial strain. This yields the following simplified equations for strain in the x, y, and z directions, respectively:

$$\epsilon_x = \frac{1}{Y}[\sigma_x - \nu\sigma_y]$$
$$\epsilon_y = \frac{1}{Y}[\sigma_y - \nu\sigma_x]$$
$$\epsilon_z = \frac{1}{Y}[-\nu(\sigma_y + \sigma_x)]$$

For our consideration of thin films, we impose the condition that the strain in the plane is equal $\epsilon_x = \epsilon_y = \epsilon_{\parallel}$ since we work in the pseudocubic approximation. We find an expression for the Poisson's ration:

$$\nu = \frac{-\epsilon_z}{2\epsilon_{\parallel} - \epsilon_z} \tag{2.4}$$

The strain is expressed as the percentage deviation of the substrate's pseudocubic lattice parameter $a_{\text{subs, pc}}$ from the bulk pseudocubic lattice parameter of the film $a_{\text{bulk, pc}}$.

$$\epsilon_{\parallel} = \frac{a_{\text{substrate,pc}} - a_{\text{bulk,pc}}}{a_{\text{bulk,pc}}} \cdot 100$$

2.4 Orbital Structure & Symmetry considerations

Most physical properties in transition metal oxides are determined by the strong interactions of the correlated electrons in the d-orbitals of the transition metal. Strong interactions need to be considered, which is why conventional band theory often fails to describe this class of materials successfully. For example, according to band theory half-filled band structures lead to a metallic behaviour. This is not necessarily the case with TMOs. Nevill F. Mott and John Hubbard have developed an understanding of these materials by taking into account strong interactions between

those electrons. In a simplified model, we consider a non-degenerate system with one electron per site. Electron correlation considers the competition between electron hopping given by the bandwidth $W \sim 2t$ modelled by tight-binding hopping and Coloumb repulsion U. If the energy gain obtained from hopping is larger than the repulsive potential ($W > U$) the material acquires metallic characteristics. On the other hand, stronger electron-electron repulsion ($U > W$) leads to localized electrons with insulating behaviour and localized magnetic moments. This leads to a two-band model. If we consider $U = 0$ and adiabatically switch on the interaction U we go from a one-band tight-binding model, where a half-filled band describes a metal to a split-band, where the half-filled band describes a *Mott-insulator* with a band gap $E_g \sim U$ [11].

The energy levels of the anisotropic d-orbitals are greatly impacted by their crystal environment. The crystal field describes the electrostatic interactions and the hybridization of the oxygen's p-orbitals in the octahedral cage with the B-cation's d-orbital [12]. Starting from the most symmetric crystal structure, the cubic structure, the atomic d-orbital is split into two energy levels t_{2g} and e_g. By grouping the symmetrically equivalent d_{xy}, d_{zx} and d_{yz} orbitals together in t_{2g} and $d_{x^2-y^2}$ and $d_{3z^2-r^2}$ orbitals in e_g [13]. By reducing the crystal's symmetry to tetragonal and then orthorhombic structure the orbitals degeneracy is lifted further (see **fig. 2.7**). The occupation of the field-split t_{2g} and e_g orbitals and the pairing of the spins determine the local magnetism of these compounds. According to Hund's law, the orbitals are filled from low to high energy such that the number of unpaired electrons is as high as possible reducing the Coloumb energy. Depending on the crystal field splitting, the spins in t_{2g} might be paired first before occupying the higher energy e_g orbitals. The spins can either be unpaired and have high spin or paired and have low spin determining their magnetic properties.

The distances between the transition metal ions and respectively neighbouring unpaired d-orbitals are usually too large to warrant exchange coupling since the exchange integral depends on the d-d orbital overlap. This is why indirect exchange dominates and exchange is mediated by the oxygen anions (*superexchange interaction*) and direct d-d hopping can be ignored. One effect of the O2p-B3d interactions is already discussed above: the crystal field splitting. The p-electrons have the strongest overlap with the 3d electrons and therefore have a huge influence on the properties of perovskites [11]. We need to consider intersite hopping via the O2p orbital (see **fig. 2.6**), with the following processes. Step 1) one 2p electron from the O^{2-} can hop to one of the overlapping TM sites (left, i) and occupy the orbital accordingly, either by pairing an occupied level (opposite spin) or occupying a higher level (same spin), depending on the crystal field splitting energy and the pairing energy. Step 2) the vacancy created in the 2p orbital can be filled by an electron hopping from the other TM-ion (right, j) to the 2p orbital [12]. Effectively, transferring the electron from site j to site i as can be seen:

$$d_i^n \, d_j^n \, p^6 \rightarrow d_i^{n+1} \, d_j^n \, p^5 \rightarrow d^{n+1} \, p^6 \, d_j^{n-1}$$

The intermediate state costs the energy Δ_{CT} considered the charge transfer gap, which is the energy required for the p-d excitation. Pauli exclusion principle, however, prohibits the electron hopping from site j to the oxygen site (in step 2) to have the same spin. Thus, depending on step 1), let's say we have a low-spin situation (as depicted in **fig. 2.6**), then the spin filling the vacancy from the site j needs to be anti-aligned with respect to site i. This would lead to an antiferromagnetic long-range order. The neighbouring sites are antiferromagnetically coupled where the effective d-d-hopping is given by $t_{dd} = -2t_{pd}^2/\Delta_{CT}$ and $J_{\text{ex}} \sim t_{dd}^2$ [12].

We have seen from the brief discussion in this section that there are many contributions to the energy competing with each other. It is clear that these energies are coupled to the spatial crystal structure giving rise to complex exchange and strong magnetostructural coupling.

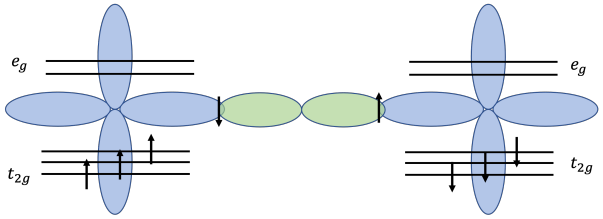

Figure 2.6: An example of superexchange interaction in which the t_{2g} orbitals are half-filled in a high-spin state. The p-orbital donates one of its paired spins. Depending on the crystal field energy, the spin state may be raised or lowered. In this case, spin-pairing might be favoured leading to an anti-parallel alignment of the spins occupying neighbouring TM-ion sites.

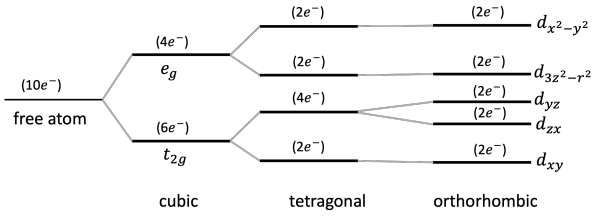

Figure 2.7: Schematic diagram of crystal field splitting in different crystal environments. By lowering the symmetry the degeneracy of the d-orbitals is lifted. The crystal field energy splitting the t_{2g} and e_g levels determine high or low spin ordering competing with Hund's pairing and depending on the number of valence electrons.

2.5 Basic properties of constituent materials

2.5.1 $LaCrO_3$

$LaCrO_3$ (LCO) crystallizes in a centrosymmetric orthorhombic (Pbnm) crystal structure with the lattice parameters a=5.513Å, b=5.476Å, c=7.759Å. The geometric tolerance factor for LCO using the ionic radii of the ions is $t = 0.85 < 0.9$. In Glazer notation, the orthorhombic distortion due to octahedral tilts is described by $a^-a^-c^+$. Along the (100) and (010) the tilts are equal in value denoted by the string 'a' and out-of-phase, while in the (001) direction the tilt has a different magnitude 'c' and is tilted in phase. A pseudocubic unit cell can be isolated with the lattice parameter $a_{pc} = 3.885$ Å which is the value that will be used in calculations in the chapter discussing the results (see **fig. 2.8** for the pseudocubic approximation). $LaCrO_3$ is in the Cr^{3+} oxidation state, thus chrome has three remaining valence electrons in the 3d orbital.

In bulk, due to crystal field splitting of the 3d orbitals in an orthorhombic crystal, the three electrons occupy the $(d_{xy})^1$, $(d_{xz})^1$ and $(d_{yz})^1$ in high-spin configuration separated by the Coloumb repulsion energy. The t_{2g} band is half-filled thus it is in a high-spin configuration, making it a *Mott-like* insulator [15].

In a strained system, the induced tetragonality leads to a degeneracy in the t_{2g} due to the increased symmetry of the system (**see fig. 2.7**). It was found that for compressive strain (LCO//LSAT) the band gap is 3.39 eV and for tensile strain (LCO//STO) it is increased to 3.65 eV [16], comparing to the bulk value of $\sim$ 3.4 eV [17]. These transitions are of the type $t_{2g} \rightarrow e_g$, which are tunable by strain. Although this bandgap might warrant a semi-conductor classification, it was actually shown after decades of debate surrounding its transport properties, that excitations across the mentioned band gap merely lead to localized excited states and no conductivity. The excitation into the conduction band by O2p $\rightarrow$ Cr3d provides the dominant contribution and is much larger $\sim$ 4.8 eV. However, it is tunable by strain [18]. It has been shown that doping with elements from group IIa increases its conductivity [19]. For compressively strained LCO doped with Sr^{3+} it is found that the material becomes a p-type semiconductor and a metal at doping levels $x \geq 0.65$ [20].

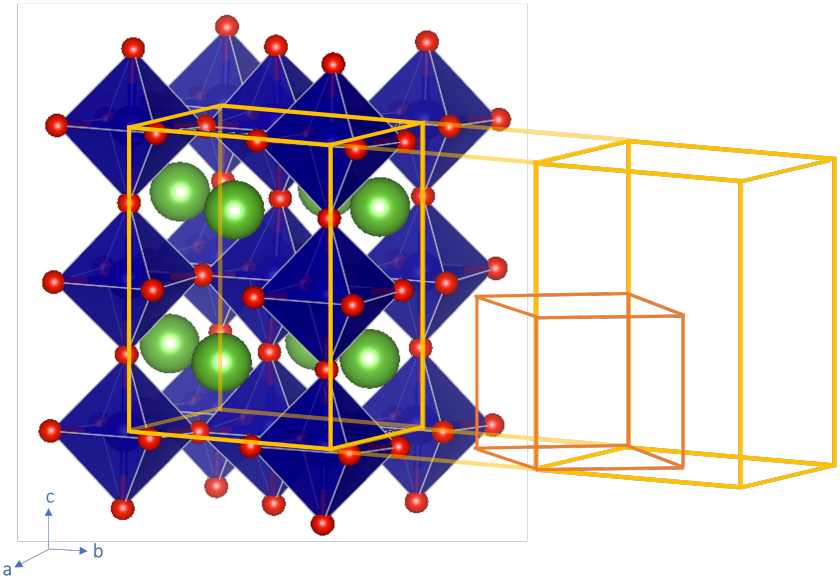

Figure 2.8: The conventional orthorhombic LCO unit cell (in yellow) and the construction of the pseudocubic unit cell (in red). Here the approximation $a_{pc} = 1/2\sqrt{a^2 + b^2}$ is made. In blue, located inside the oxygen octahedron, is Cr. In green is La coordinated by 12 oxygen ions indicated by the green polyhedron. In red are the oxygen ions. Image credit: VESTA [14]

LCO is a G-type antiferromagnet and displays a weak antipolar displacement of its Cr atom [21]. The Néel temperature in bulk is close to room temperature at $T_N \sim 290K$ [22]. The local non-centrosymmetric environment promotes antisymmetric exchange interaction mediated across the $Cr^{3+}-O^{2-}-Cr^{3+}$ bond leading to antiferromagnetic non-collinear spins. Because of the resulting net magnetic moment, it is considered a weak ferromagnet. The magnetic anisotropy and the net magnetic moment are tunable by strain. It is found that with compressive strain the easy axis is in the out-of-plane direction while it is in-plane for tensile strain as well as for the relaxed case [16]. The magnetic moment is also increased for compressive strain. All of which point to a strong dependence of the magnetic properties on lattice strain. The imposed strain greatly affects the octahedral distortions and thus the bond angles and bond lengths between the oxygen ion and the chromium ion and with that its optical, electronic and magnetic properties.

Because of competing magnetic anisotropy energies of the film itself and the surface/interface, strained epitaxial LCO films undergo a spin reorientation transition at a critical thickness t_c. It was shown for the tensile strained LCO//STO that $t_c \approx 60$ nm, where for $t < t_c$ the spin axis is oriented along the c-axis and for $t > t_c$ the spin axis is in the ab-plane [22].

2.5.2 $SrCrO_3$

$SrCrO_3$ (SCO) exhibits an undistorted cubic perovskite structure at high temperatures with lattice parameter a = 3.811 Å and a low-temperature transition to a tetragonal structure at $T_N \approx 40$ K, associated with C-type antiferromagnetism with lattice parameters a = 3.821Å and c = 3.794 Å [23, 24]. SCO is in the Cr^{4+} oxidation state and Cr has the electron configuration d^1_{xy} $(d_{yz}, d_{zx})^1$ due to its tetragonal structure (see **fig. 2.7**). The valence of Cr^{4+} is especially hard to stabilize since it is very sensitive to the growth conditions [23, 24]. This is why there are inconsistent and contradictory reports surrounding its electronic properties. Most recent articles indicate that SCO is a metal in bulk [25]. Powder neutron diffraction has shown half-order peaks indicating C-type AFM order [25]. As of today, bulk SCO is considered metallic and antiferromagnetic in its ground state. In thin film growth, only a small window of oxygen to argon ratio has been found to stabilize this phase [26]. Metallicity and indications for antiferromagnetism in the ground state of thin films have been reported [20]. Furthermore, strain-driven metal-to-

insulator transitions have been observed due to strain-stabilized Jahn Teller distortions lifting the degeneracy in $(d_{yz}, d_{zx})^1$ facilitating the opening of a band gap [26, 21]. Measurements done by our own group on SCO thin films include resistance measurements showing metallic behaviour in compressively strained (-0.68%) systems (see **fig. 4.20d**) and metal-to-insulator transitions for larger strains (not presented). XMCD as well as SQUID magnetometry measurements exclude a ferromagnetic phase in these films. Low energy muons have detected a magnetic phase transitions at temperatures $\sim 130\,\mathrm{K}$, much higher than what was previously reported $T_N \sim 40\,\mathrm{K}$ [25]. The XMCD, SQUID and muon results are not presented in this work.

Chapter 3

Methods

3.1 Epitaxial thin film growth

Epitaxy is the growth of crystalline material on top (*epi* greek) of a crystalline substrate. The substrate imposes a crystalline order (*taxis*) on the material above. The right conditions need to be met for the successful and high-quality growth of each compound. In the category of physical vapour deposition (PVD), there are different deposition techniques: molecular beam epitaxy (MBE), pulsed laser deposition (PLD) and plasma sputtering deposition. In all of these methods no chemical reactions, but a physical mechanism, to create and transport the gaseous phase of the target material to condensate on the substrate, is involved [9]. The substrate has to be structurally similar and its lattice constant has to be relatively close to the materials bulk form for the adsorbed gas to nucleate and crystallize in the desired two-dimensional structure. In the case of dissimilar materials, the deposited material might not be bonded strongly enough to the substrate [27]. The mismatch of the lattice parameters between the substrate and the film will impose a strain on the film and it will adopt the substrate well defined crystallographic orientation.

3.1.1 Magnetron Sputtering Deposition

In sputtering deposition, the source material for the film growth is ejected from a stoichiometric ceramic disk (target) by the bombardment of argon ions. The removal of the target atoms is referred to as sputtering. The process results from kinetic energy transferred from the ions accelerated by the electric field to the atoms in the ceramic target. The sputtering yield highly depends on the kinetic energy of the incoming ions. In the right kinetic energy range called the "knock-on" regime ($50 - 1000\,\mathrm{eV}$), the impinging ions will cause a chain of collisions, where the target atoms will knock each other out of the surface [9]. The target (cathode) and the anode, the electrodes, generating the ionizing alternating electric field are located on one axis in the growth chamber. If the target material is an insulator, an alternating field is needed because the accumulation of positive charge on the target would cancel out the electric field. The substrate is located off-axis (by 90° with respect to the cathode anode axis) on the temperature-controlled heater to avoid sputtering of the deposited material [9]. This off-axis geometry reduces the deposition rate since most ejection of particles happens on the target's axis. The alternating field uses high frequencies in the RF regime, such that only electrons are light enough to respond to the fields. The reason that the Ar^+ still bombards the target is that the cathode has a smaller area than the anode, such that after a few cycles, the electrons that land on this area will lead to a higher electron concentration and thus a net negative bias, which is what the Ar^+ see [9]. A dc setup with the target and substrate on the same axis is possible for metal sputtering since charge build-up is not a problem. The system, as described so far, is not complete yet. To improve the plasma efficiency and the deposition rates, strong magnets are located behind the target in such a way that, together with the electric field, they constrain secondary electrons being emitted

from the target surface, which helps sustain the plasma [28]. Trapping the electrons close to the target surface leads to larger ionisation efficiency and denser plasma, increasing the sputtering rates. Until now, it was implicitly assumed in this text that the sputtering yield is independent of the elements in the target, which is not true. Some elements are sputtered more easily than others (*preferential sputtering*), leading to the depletion of easily sputtered elements on the target's surface [9]. Not only that but also oxygen bulk diffusion in the target or adsorbed oxygen on the surface can influence the surface composition [29]. By sputtering the target, prior to inserting the substrate inside the chamber for the growth, the problem of preferential sputtering can be overcome. After some sputtering time, the content of the easily sputtered elements will be lowered and steady-state will be reached. A few minutes of presputtering will resolve the problem; for the other issues mentioned, presputtering might take hours [29].

Some samples require post-growth treatments to fill oxygen vacancies in the film. At elevated temperatures, diffusivity is increased, and the oxygen vacancies can be replenished by annealing with an oxygen atmosphere. The oxygen vacancies affect the lattice parameter if a critical concentration level is reached [30]. This effect can be quantified by using x-ray diffraction characterization (more on that in section 3.2.2) pre and post-annealing.

Substrate

The importance of the substrate should not be understated. Ideally, the substrate offers nothing but mechanical support to the heterostructure. Of course, in most cases, that is not true, and the substrate affects the quality of the film and its physical properties, which is often desired when studying physical processes. The film and substrate need to match well in lattice parameters and atomic positions. Luckily, there is a wide range of high-quality perovskite oxide substrates that cover a wide range of lattice constants that are commercially available. For a high-quality single crystal film growth, it is a requirement that the substrate consists of an atomically flat "step-and-terrace" surface [9]. If the steps are of equal height corresponding to one unit cell, one can assume that the terminating layer in all steps is the same. The quality of the starting surface and the absence of any roughness are crucial to avoid structural defects [31]. The commercially available substrates are typically polished. They often require to be treated by annealing at high temperatures sometimes purely in oxygen or in air. The annealing procedure recrystallizes the surface layer and planarizes the polished surface [9].

Growth parameters

Several parameters can be optimized to achieve coherent epitaxial growth. These parameters include the temperature of the substrate, the pressure inside the chamber, the composition of the gas(es) and their flow into the chamber as well as the RF power. Next to the Ar gas for the growth of oxides, there is often also O_2, to assure the oxygen stoichiometry of the film [27]. The gas pressure needs to be sufficiently high in order for the plasma to be generated [28]. Larger chamber pressures also improve the thermalization of the ejected particles leading to more uniform growth [9]. As mentioned above, the sputtering rate is highly dependent on the plasma and in turn on the RF power. By increasing the power, the sputtering rates and, thus deposition rates increase. Therefore, by varying the power, one can change the growth rate of the film. Some oxides require high temperatures $500 - 900^\circ$ C. Such temperatures are needed for obtaining the desired crystal structure, phase, domain structure, and lattice orientation, or to improve crystallinity [9].

Chamber & components

The growth chamber is designed for ultra-high vacuum (UHV) use even though sputtering requires a certain atmosphere. The UHV design prevents and reduces any outside contamination to the chamber and enables vacuum annealing or vacuum cooling. The chamber remains sealed

at all times, except for exchanging the targets. The samples are removed or inserted via a load lock, which is pumped independently and is decoupled from the chamber. The load lock is pumped with a turbo pump and a scroll pump as the base pump. The substrates are pasted to a heater with silver paste for uniform heating. The resistive heater is temperature-controlled and equipped with a thermocouple for temperature read-out. The O_2 and Ar gas inlet into the chamber is mass flow controlled. A turbo pump and a base pump continuously pump the chamber. A butterfly valve and a leak valve are used to adjust and maintain constant pressure during the growth. The chamber pressure is read out using pressure sensors, a membrane pressure sensor for high pressures and a Pirani/Cold cathode sensor for low pressures. The RF power, the mass flow, the temperature, the butterfly valve and the sputtering time are all controlled and monitored via a LabVIEW program on the lab computer.

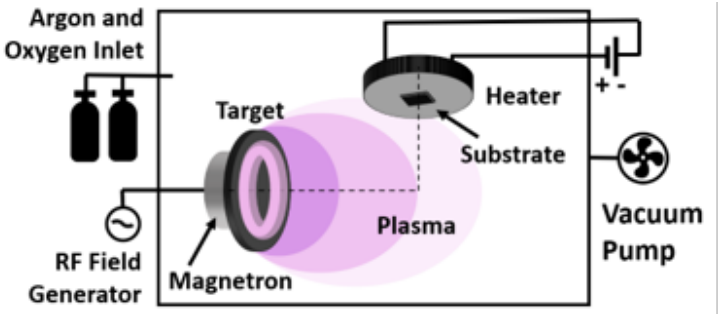

Figure 3.1: Schematic sketch of the vacuum chamber and its components

3.2 Characterization Techniques

3.2.1 Atomic Force Microscope

The atomic force microscope (AFM) is an instrument that stands for a wide range of imaging modes, we are interested in the most basic types capable of measuring the topography of the films. The resulting image is a three-dimensional height map of the sample surfaces down to atomic resolution. We are interested in these images because they enable us to see if our films have uniformly grown in a layer-by-layer manner. In the following, the basic concepts, measuring modes and components of an AFM instrument are discussed, followed by a brief discussion on data and image processing. Please refer to the textbook referenced in [32] for more detailed explanations.

Basic concepts and modes

The height map is created by tracing the surface in a scanning raster manner with a probe attached to a cantilever that acts like a spring. This may be achieved in different ways, either the probe is in direct contact (contact mode) with the surface or it traces the surface at a distance where it is still sensitive to force interactions (non-contact mode). The probe-surface interaction lies at the heart of the operation and depending on their relative distance either repulsive or attractive forces dominate (see **fig 3.2**).
To understand the working principle of the AFM, we first discuss the simplest mode, which is the constant height contact mode. No feedback system is required and the cantilever height simply stays constant during the scanning process. The profile is recorded by measuring the deflection of the cantilever. This deflection is recorded by tracking the reflection of a focused laser onto the cantilever in a photo-diode array (see **fig 3.2**). The deflection is then translated to changes in height. This method is the basis for the development of more advanced modes, such as the most commonly used version of contact mode, where there is a set parameter that

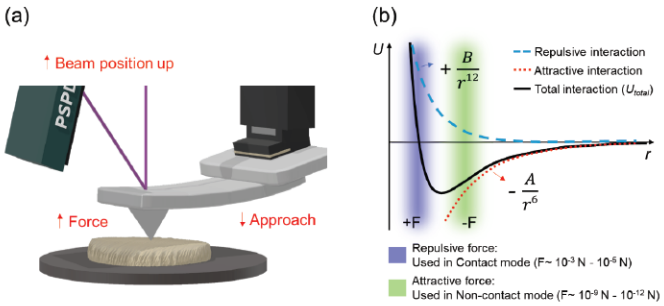

Figure 3.2: a) the basic set-up of the laser system used in both contact and non-contact AFM modes, b) force-distance curve depicting the repulsive regime due to the overlap of electron orbitals and the attractive regime due to Van der Waals interaction. Reprinted from the Park Instruments website [33].

the feedback system corrects for: the spring force exerted on the cantilever given by Hooke's law

$$\vec{F} = -\vec{k}_0 \cdot \vec{D} \tag{3.1}$$

where k_0 is the spring constant and D is the deflection. The feedback system will finely adjust the cantilever's z-position with a piezo transducer until the set value is restored. The amount the z-position was corrected for reflects the change in height of the profile.
Non-contact mode operates in the attractive regime between probe and surface (**fig 3.2**). Here the cantilever hovers over the surfaces and oscillates, driven by a piezoelectric element. The operational frequency f_{op} is chosen close to the resonance frequency of the cantilever given by $f_0 = \sqrt{k_0/m}$. At this frequency f_{op} the set-value of the amplitude A_{set} is given by the resonance curve of the cantilever, which is obtained by performing a frequency sweep. The attractive interaction with the surface causes a negative shift of the resonance frequency given by the positive sign of the gradient of the force normal to the surface

$$f' = \sqrt{\frac{k_o - \frac{\partial F}{\partial z}}{m}} \tag{3.2}$$

effectively changing the amplitude and phase once the probe interaction with the surface changes. Either amplitude or phase can be used as the set parameter for the feedback loop. The oscillation is monitored using a lock-in amplifier. The lock-in amplifier is part of the feedback system and compares the measured oscillation obtained from the photo-diode array to the set oscillation and determines the phase or deviation in amplitude.

Components

The atomic force microscope is composed of the microscope stage, the control electronics and the computer (see **fig. 3.3**). The microscope stage includes the scanner consisting of the cantilever with the scanning probe, the sample stage, the laser and the photo-diode array as well as the optical microscope. For the scanning procedure, three piezoelectric transducers control accurate movement on the Ångstrom scale in three dimensions, either by manipulation of the sample stage or the scanner. In basic terms, a piezoelectric transducer converts electrical potential into mechanical motion and vice versa.

The control electronics is at the interface between the microscope stage and the computer with the particular software to acquire and display AFM images as well as control acquisition parameters such as scan speed, gains and set-point. The gains determine the response of the feedback system handling the error value, which is the difference between the set point and the

measured value. To minimize the error the control variable (z-height) is adjusted. The control electronics produce the output signals that drive the z-piezo and process the incoming signals from the photodiode in the feedback system comparing them to the set values.

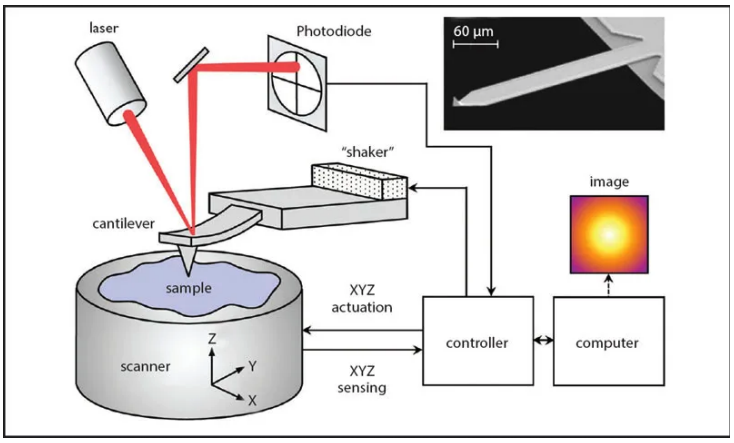

Figure 3.3: Schematic drawing of the AFM components and the communication paths. Reprinted from Tech briefs [34]

Taking AFM images & processing

The user starts their measurement with the optical alignment, adjusting laser and photodetector positions if necessary. The sample is positioned using the optical microscope. Once the tip is engaged, the acquisition parameters can be optimized while the scan remains in line scan, meaning it is fixed to a one-dimensional direction. In this setting, the user compares forward and backward scans and keeps an eye on the error signal as the gains are adjusted. In contact mode, the error signal is given by the deflection, since the feedback system cannot perfectly respond. While in non-contact mode the error signal is either given by the phase or the amplitude. Once the user is satisfied, the two-dimensional scan can start. The resolution of the features on the surface is solely given by the tip. If the tip gets worn down the shape of the tip limits the resolution and will be convoluted with sharp and large peaks, visible in the image. The user has the possibility to determine the digital resolution, namely the number of pixels per line, which will affect the scanning time. Our images were taken with our group's Park's NX10.

The raw images contain three-dimensional information. The goal of image processing is to adequately extract information on features that were measured and handle measurement artefacts in the right way. The raw data is unleveled, meaning it might be distorted due to instrument artefacts or very high objects on the surface. Therefore, the raw data is first flattened by subtraction of an adequate background. This is done by an algorithm fitting a polynomial line-by-line and subtracting it from the data. Furthermore, in order to be able to correctly interpret the step height in our thin film images, a plane is fitted by three points defined by the user. The plane is subtracted and now the colour map corresponds to the true height. It is possible to take line profiles to determine the height of the steps. The images were processed using the Gwyddion software.

3.2.2 X-ray diffraction (XRD)

X-ray diffraction is the primary method for structural analysis of thin films down to sub Ångstrom scale. It is a powerful tool for the structural characterization of the film because its versatility allows for extensive analysis regarding the quality of the film, interface roughness, thickness, lattice parameters, strain and crystalline phase [35]. For diffraction, we use monochromatic and parallel X-rays to irradiate our thin film. The set-up is rather simple and explained in figure 3.4. We have two axes, ω defines the angle for the incoming x-rays and 2ϑ defines the

detector angle. ψ and R_x are the remaining degrees of freedom, relevant for sample alignment or the diffraction measurement.

Under kinematic conditions and elastic scattering, we have Bragg's law for constructive interference from a reflecting family of planes

$$n\lambda = 2d_{\mathrm{hkl}}\sin(\vartheta) \qquad (3.3)$$
$$n = 1, 2, 3, ...$$

where λ is the x-ray wavelength and in the same order of magnitude as the lattice parameters, ϑ is the Bragg angle, n is the order of reflection and d_{hkl} is the spacing of the reflecting family of planes. In reciprocal space, Laue's equation equivalently describes the scattering condition

$$\vec{k}_{\mathrm{in}} - \vec{k}_{\mathrm{out}} = \vec{G} \qquad (3.4)$$

where the difference between the incoming and scattered x-ray is equal to a reciprocal lattice vector $\vec{G}$. Since we have elastic scattering it follows from energy conservation, that

$$|\vec{k}_{\mathrm{in}}| = |\vec{k}_{\mathrm{out}}| \qquad (3.5)$$

With thin films, we are usually interested in the out-of-plane lattice parameter. We perform a symmetrical $\vartheta/2\vartheta$ scan around the respective Bragg peak (001) or (002) c = $d_{(001)}$ or c = $2d_{(002)}$ of the substrate. The spacing between planes for a cubic lattice is given by

$$d_{\mathrm{hkl}} = \frac{a}{\sqrt{h^2 + k^2 + l^2}}$$

The detected intensity is proportional to the number of planes which is why in the case of thin film samples the detected signal will give rise to a strong Bragg peak coming from the substrate ($N_{\mathrm{sub}} \to \infty$) and a faint peak due to the finite number of unit cells N accompanied by thickness fringes or Laue fringes due to constructive interaction form the N reflecting thin film planes. The Laue fringes are a good indication of the quality of the film. By fitting them one can determine the number N of reflecting planes from the oscillation period and the c-axis from the angular position ϑ and thus determine the thickness of the film. Deviations of the c-axis with respect to the bulk are expected for a strained film and are an indication of the strain and stress applied to the film. To determine the true strain between the substrate and the epilayer, in-plane structural information is needed (more on that below).

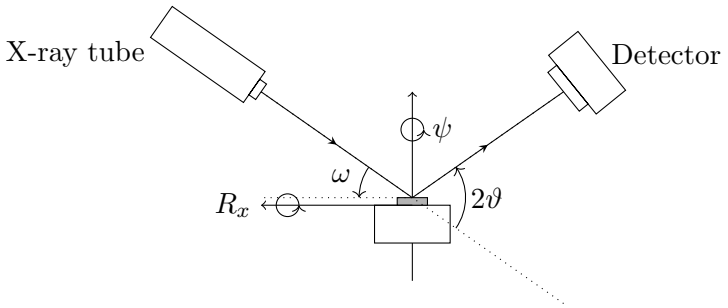

Figure 3.4: Schematic set-up of x-ray diffraction, the angles and the degrees of freedom.

Superlattices

Superlattices are periodic structures consisting of repetitions of the same bilayer. Superlattices can also consist of more than two repeating layers. The new wavelength Λ is given by

$$\Lambda = \sum_i n_i c_i \qquad (3.6)$$

where ideally n_i are integers corresponding to the number of layers and c_i are the c-axes of the different materials involved. The periodic structure will fulfil Bragg's law

$$2\Lambda \sin(\vartheta_n) = n\lambda \tag{3.7}$$

The reflecting planes of the individual layers in the superlattice have different spacing so the main peak or the zero-order peak will reflect the average c-axis $\tilde{c}$. This peak will be accompanied by satellite peaks, the higher-order peaks. Λ is determined from the linear relationship between the positions ϑ_i of the satellite peaks vs the order n. In principle, the same measurement can be done as with a thin film. The intensity and the number of satellite peaks are an indication of the film's crystalline quality such as interfacial roughness between the layers.

Other measurement modes

Reciprocal space maps are two-dimensional intensity maps in reciprocal space where not only the out-of-plane momentum is probed but also the in-plane component by measuring the intensity around a reciprocal lattice spot corresponding to a crystallographic direction containing in-plane lattice information. This is done by an asymmetric $\omega/2\vartheta$ configuration. The area around the reflection point (hkl) is scanned by performing $\omega - 2\vartheta$ scans. The additional information reveals the strain state of the film. For a coherently strained film, we expect the in-plane lattice parameters to adapt to the in-plane lattice of its substrate. Any distortions along the in-plane direction in the map point to the relaxation of the film.

Instrument

The instruments equipped for high-resolution XRD consist of a high-flux X-ray source, the incident optics, the goniometer, the receiving optics and finally the detector. The X-rays are generated in a vacuum tube by accelerating electrons created by thermionic emission from a tungsten cathode to a copper anode, which gets ionized. Upon relaxation of the excited electrons photons with characteristic wavelengths are emitted. The most intense lines of the emission spectrum are the K-lines. The generated X-rays exit the vacuum tube via beryllium windows as a line or spot. However, to obtain high-resolution data necessary for analyzing thin films the X-rays need to be monochromatized and collimated. The incident optics consist of a parabolic multilayer mirror, which is an artificial heterostructure consisting of alternating low and high-density layers designed to collimate the X-ray beam, which needs to be carefully aligned. The multilayer mirror is constructed such that it satisfies Bragg-law for the incoming x-rays and by that works as a wavelength selector and monochromator. The layer thickness of the heterostructure varies as a function of the parabola and determines the outgoing angle of the diffracted x-rays [36]. The divergence of the beam in the horizontal direction remains unaffected. A length limiting slit and an incident slit control the size of the beam in the horizontal direction before it arrives at the sample and two receiving slits and a soller slit, reduce the divergence at the detector. [35]. Nevertheless, the parabolic multilayer mirror cannot discriminate between the $K_{\alpha 1} = 1.54059\,\text{Å}$ and $K_{\alpha 2} = 1.54443\,\text{Å}$ wavelengths, it does, however, work as a filter for the K_β component, Bremsstrahlung and background emission [35]. This is why the high-resolution Ge(220) 2-bounce monochromator is necessary for the selection of the desired $K_{\alpha 1}$ line at the expense of intensity.
As briefly mentioned above, the goniometer controls the angles and degrees of freedom. Next to the $\vartheta/2\vartheta$ angles the sample stage can move in the z-direction and rotate along ψ and tilt along R_x. Which are the parameters that need to be aligned before the measurement takes place (see **Fig.** 3.4). The diffracted X-rays are converted to an electrical signal by the detector in the units of counts per second (cps). High-intensity X-rays, from the substrate peak or from the direct beam, while aligning the optics, should be avoided, as they can damage the detector or lead to a saturated response. Attenuators, in the form of thin metal foils, are automatically employed

when the intensity reaches a certain value to protect the detector.
Our measurements were done with Rigaku's Smartlab from the Chemistry department.

3.2.3 SQUID magnetometry

The superconducting quantum interference device (SQUID) sensor is the most sensitive device to detect changes in magnetic flux. Superconducting pick-up coils surrounding the sample are inductively coupled to the SQUID. Local field changes at the sample are not directly detected by the SQUID sensor but by the pick-up coils (as depicted in **fig. 3.5**).

In dc- or vibrating sample-mode (VSM) the magnetized sample is moved mechanically along the axis of the applied field inside a second-order gradiometer consisting of these superconducting pick-up coils (**fig. 3.5**). The movement leads to a change in flux across the coils inducing a current. There are two coils oppositely wound such that the induced voltage coming from changes in the externally applied uniform field during ramping will cancel each other out.

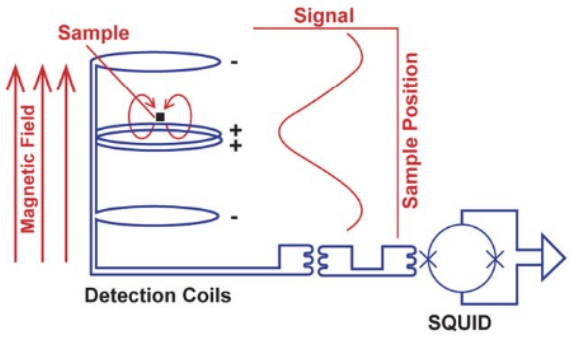

Figure 3.5: Schematic diagram of the SQUID detection system. The sample is moved within the superconducting pick-up coils on the axis of the externally applied field. The pick-up coils are inductively coupled to the shielded SQUID. Variations in fields induce screening currents in the detection coils, which are nulled by the SQUID feedback currents yielding the actual SQUID voltage. Image credits: MPMS3 manual

To understand the working principle of the SQUID one needs to understand the underlying quantum mechanical mechanisms first. The first principle is flux quantization: the magnetic flux inside a superconducting ring will be trapped and variations to the flux happen in a discrete manner with the smallest change possible, being that of the flux quantum ($\phi_0 = 2.068 \cdot 10^{-15}$ W) [37]. The second is, that if the superconducting ring consists of a 'weak link', a section where the superconductor is replaced by an insulating material, the ring becomes a Josephson junction, named after its theoretical predictor. If the insulating sector is smaller in thickness than the superconducting correlation length, the electrons can tunnel across the junction. Up to a critical current, there is no voltage drop across the junction. Currents larger than the critical current promote the system to a normal/resistive state (**fig. 3.6**). In the regime of the critical current in the I–V curve, the variation $\partial V/\partial I$ is large and changes in magnetic flux will lead to screening currents causing variations in the measured voltage. The current is thus converted to voltage, which is periodic in the flux quantum ϕ_{ext}. An external feedback system, which is inductively coupled to the SQUID, is used to null the induced currents in the detection coil. This feedback voltage is the actual SQUID signal.

The SQUID response as a function of position in the gradiometer (dc) or time (VSM) is fitted to a dipole magnetic moment with sign and value remaining constant [37]. It is only the vector component along the field that is extracted [38]. In the VSM mode, there are additional measurement parameters such as the frequency, amplitude, and measurement time that one has to account for. In both modes, however, the shape and size of the sample play a role, as the machine is calibrated against a cylindrical Palladium rod, according to Quantum Design's application notes [39, 40]. At low applied fields the accuracy of the applied field is limited by

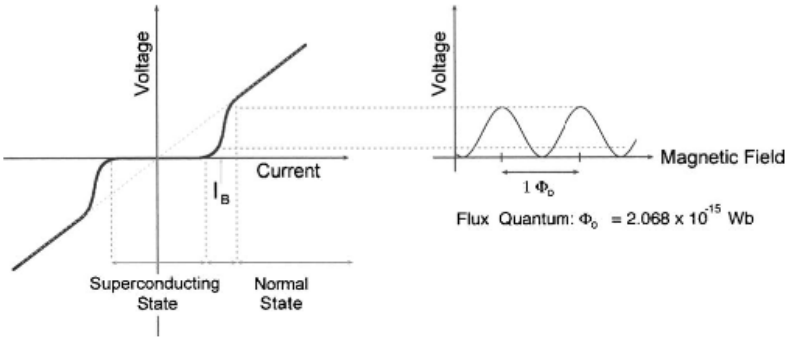

Figure 3.6: The I-V curve of the Josephson junction. Current applied close to the critical current promotes the system to a superconducting state. On the right the V-ϕ curve is depicted: the induced currents by the changing fields lead to an oscillation of the voltage measured periodic in the flux quantum ϕ_0. Image credits: reference [37]

some remnant field in the superconducting magnets caused by magnetic flux pinning in type II superconductors [38].

Instrument

Two very important components of the magnetic property measuring system (MPMS), next to the measuring system, are the temperature control and the magnetic field control system. The temperature control module (TCM) allows for both continuous and stable operations in a temperature range of 1.8 K - 400 K. The regulation of the heater currents is based on a PID feedback system. This system also reports the sample temperature using different thermometers and applies corrections due to field, location, thermal history and thermal conduction. The cooling is monitored by the gas handling controller (GHM). Cooling occurs by drawing helium gas into the annular space around the sample chamber, where it evaporates, with the use of a vacuum pump. The MPMS dewar consists of the liquid helium tank surrounded by vacuum insulation embedded inside the liquid nitrogen tank, which is insulated against thermal radiation. The purpose of the liquid nitrogen layer is to reduce liquid helium boil-off. Additionally, the dewar is isolated against vibration. Not only is the helium needed to cool the sample it is also used to cool the NbTi solenoid (magnet) that produces a vertical field ranging from -7 T to 7 T and the magnet systems (quick switch and leads), as well as the SQUID and the superconducting magnetic shield (around the SQUID) and the superconducting detection coils. The current for the magnet is supplied by the superconducting magnet controller (quick switch) via current leads. Above its critical temperature, it generates a voltage across the magnet. The rate at which the solenoid current and the magnetic field change in the magnet is given by this voltage and inductance of the solenoid. Our measurements were done with Prof. Thomas Greber's Quantum Design MPMS3 and the above information is taken out of Quantum Design's manual.

3.2.4 Electronic transport

The electronic transport properties of the heterostructures were determined by using the Van der Pauw measuring technique. This method allows for the measurement of the resistivity of any arbitrarily shaped sample as long as the following conditions are fulfilled

1. The contacts are at the circumference of the shape
2. The contacts are sufficiently small
3. The sample exhibits a homogeneous thickness

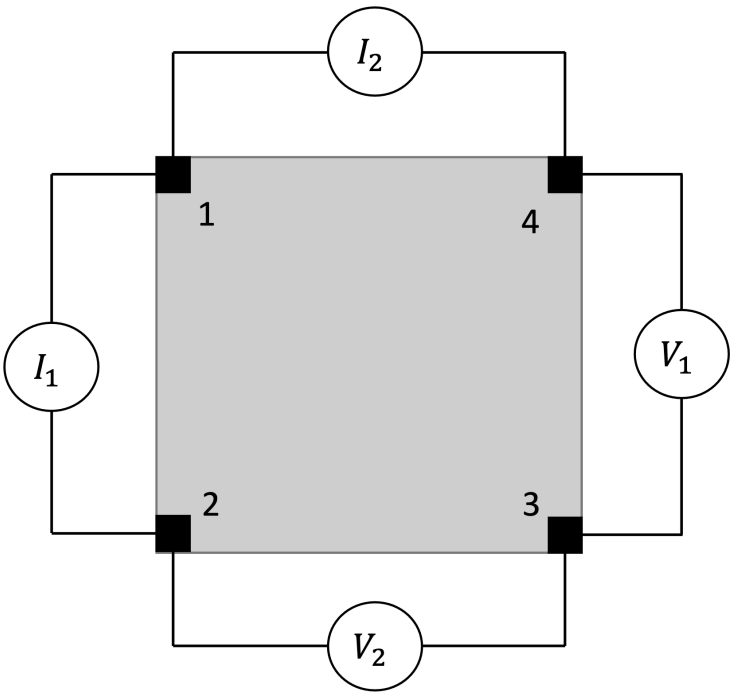

Figure 3.7: Schematic depiction of Van der Pauw measurement geometry. The voltages V_1 and V_2 are measured and the currents I_1 and I_2 are known. $R_1 = V_1/I_1$ and $R_2 = V_2/I_2$.

4. There are no holes in the sample

and the thickness of the sample is known. Four contacts are needed for the measurement. The current is applied to contact 1 and 2 and the voltage is measured at 3 and 4 leading to the resistance R_1. Then current is applied to 1 and 4 and the voltage is measured at 2 and 3 and we have R_2 (see **fig. 3.7**). It was shown by L. J. Van der Pauw in 1958 that the following relation holds

$$\exp\left(-\pi R_1 \frac{d}{\rho}\right) + \exp\left(-\pi R_2 \frac{d}{\rho}\right) - 1 = 0 \tag{3.8}$$

where ρ is the resistivity and d is the thickness of the sample. The resistance measurements are done over a temperature range since we are generally interested in the transport behaviour as a function of temperature $R_1(T)$ and $R_2(T)$. To obtain the resistivity at a temperature T_0, typically room temperature, equation 3.8 is numerically solved for $\rho(T_0)$ by plugging in the measured values of $R_1(T_0)$ and $R_2(T_0)$ and the known thickness d. The resistivity and the resistance are related by the geometric factor:

$$\rho(T) = \text{geometric factor} \cdot R(T)$$

we can now determine the geometric factor and find the resistivity $\rho(T)$ of our sample:

$$\rho(T) = \frac{\rho(T_0)}{R(T_0)} \cdot R(T)$$

from the resistance measurements.

Instrument & measurement procedure

The transport measurements were performed in-house using our experimental setup. The customized set-up consists of a motorized dipstick that lowers the sample into liquid helium. A thermocouple is thermally connected to the sample via copper and is used to monitor the temperature for constant cooling and warming rates as well as log the resistance as a function of

temperature. The four contacts are sputtered with a dc magnetron sputtering system using a shadow mask. The sample is then wire bonded to a PCB and fixed to the dipstick with screws. A Keithely source-meter-unit provides the current source and voltage meter. The measurement and the equipment are monitored via LabVIEW.

3.3 X-ray absorption spectroscopy (XAS) & magnetic circular dichroism (XMCD)

X-ray absorption spectroscopy (XAS) measurements are done at a synchrotron facility with tunable photon energies in the soft-x-ray regime (400-1800 eV). The photon energy is varied while probing the material of interest. At specific energies of the x-rays corresponding to binding energies of the electrons in the material, the absorption coefficient is increased, which is called the absorption edge. At these specific energies, electrons are excited into unoccupied states above the Fermi level, the photon is absorbed and a photoelectron is created, followed by relaxation processes (on a femtosecond 10^{-15} s timescale) releasing secondary electrons or photons of a characteristic wavelength corresponding to the involved energy levels. These edges are named K-, L- and M-edge corresponding to the principle quantum number of the core levels n = 1, 2, 3, the energies at which the absorption occurs. The absorption edge energy is shell specific, which is element-specific, i.e. with a chosen photon energy we can probe a specific element in a material. In the following, we will discuss these concepts in relation to the 3d transition metals, for which the $p \rightarrow d$ transitions are examined at the L_2 ($2p_{1/2}$) and L_3 ($2p_{3/2}$) edge.

Furthermore, the binding energies are site-specific, meaning they are dependent on the crystal field environment and chemical bonds, which result in characteristic features that are reflected in the spectrum allowing for the identification of the valence states.

The photon irradiating the sample carries momentum and the initial core of the excited electrons has a well-defined symmetry determining the interaction. The final states of the excitation process is given mainly by the dipole transition rules which is the dominant contributing effect in the description of light and matter interaction. The final state quantum numbers j, m, l and s are determined by:

$$\Delta j = 0, \pm 1;\ \Delta s = 0;\ \Delta l = \pm 1;\ \Delta m = \begin{cases} +1 & \text{left circular} \\ 0 & \text{linear} \\ -1 & \text{right circular} \end{cases}$$

The use of circularly polarized light can be used to probe the magnetic valence state. X-ray magnetic circular dichroism (XMCD) is defined as the difference of the spectrum obtained in the parallel and antiparallel configuration of the photon spin (or helicity) with respect to the direction of the applied field:

$$\text{XMCD} = \mu^+ - \mu^-$$

where μ are the respective spectra obtained with parallel (+) and antiparallel (-) polarized x-rays with respect to the applied field. The absorption is dependent on the magnetic state of the material. The unoccupied valence state in ferromagnetic materials is spin-split and thereby acts as a spin-polarized detector and an orbital momentum detector. The momentum transfer by the photon to the photoelectron is opposite for left and right circularly polarized light. For the oppositely coupled spin-orbit split levels with j = 3/2 and j = 1/2, the spin-polarization will be opposite at the two edges. The resulting XMCD peak intensity is proportional to the magnetic moment of the probed shell. By applying the sum rules, the individual orbital and spin contributions can be resolved.

In XAS, the total electron yield (TEY) is measured from the surface of the material as the electrons do not exit the sample. Additionally, the total fluorescence yield (TFY) can be

measured with photodiodes. This is based on a strong assumption that the TEY corresponds to the absorption, the more electrons are measured the more photons are absorbed, effectively probing unoccupied electronic states. By additionally resolving the energies of the emitted electrons or the characteristic wavelength the method would be extended to x-ray emission spectroscopy and resonant inelastic x-ray spectroscopy, which are not in the scope of this thesis.

Since we will be presenting one x-ray photoelectron spectroscopy (XPS) spectrum in the results subsection 4.2.3 the main difference will be mentioned here. In XPS the electrons overcome their binding energies and exit the sample surface where their kinetic energy is analysed. From the information obtained from the analysed kinetic energies of the detected electrons, their binding energy in the material is inferred. Thus, the XPS spectrum gives a direct indication of the binding energies of the occupied electronic levels.

Chapter 4

Results & Discussion

In this chapter, the results are presented and discussed. From the structural characterization of the strained LCO thin films discussing its quality and structural changes by determining the c-axis via x-ray diffraction, to the surface morphology of the layered structure imaged by atomic force microscopy, to the valence state studied by XAS and XPS, the resistivity and finally the magnetic properties. All as a function of misfit strain. We conclude the successful synthesis of LCO thin films and showcase some preliminary structural characterizations as well as electronic characterizations of the first LCO/SCO superlattices.

4.1 Growth conditions

The growth of the LCO samples presented in this thesis was optimized in the conditions needed to stabilize the Cr^{4+} of the SCO in order to ultimately grow superlattices. The suitable conditions for SCO are limited to a very small window. The target was commercially bought and characterized by SEM and EDX, confirming its stoichiometry. The samples were synthesized by RF off-axis magnetron sputtering at a chamber pressure of 0.045 mbar with 0.015 sccm oxygen flow and 150 sccm argon flow into the chamber. SCO is highly sensitive to the oxygen content, which is why accurate control of the oxygen flow is crucial for the fabrication of superlattices. This does not seem to be the case for LCO as it was also grown and characterized by us at higher contents (0.11 sccm O_2) without a problem. The substrate temperature during the growth was 750° C. A short increase (30 min) in temperature to 800° C prior to growth is conducted to make sure that any volatiles that would outgas at the growth temperature has outgassed. The rf power was 35 W leading to a very fast growth rate of about 10 s/uc. After the growth was completed the sample was cooled in a vacuum. As will be shown in the following chapters, these growth conditions yield high-quality crystalline samples. The presented LCO samples were not annealed unless specifically mentioned. All the SCO heterostructures were annealed. In the annealing procedure, the sample is heated to 250°C in an oxygen atmosphere for 5 hours.

Substrate	Crystal Structure	Orientation	a [Å]	b [Å]	c [Å]	a_{pc} [Å]
$DyScO_3$ (DSO)	Orthorhombic (Pbnm)	(110)	5.44	5.71	7.89	3.949
$SrTiO_3$ (STO)	Cubic (m3m)	(001)	3.905			
LSAT	Cubic (m3m)	(001)	3.868			
$NdGaO_3$ (NGO)	Orthorhombic (Pbnm)	(110)	5.43	5.5	7.71	3.859
$LaAlO_3$ (LAO)	Rhombohedral (R3c)	(001)	5.365	5.365	13.111	3.821

Table 4.1: Summary of the substrates used and their crystal structure, orientation, the lattice parameters as well as corresponding pseudocubic lattice parameters. Due to lack of space, the chemical formula for LSAT is given here: $(LaAlO_3)_{0.3}(Sr_2AlTaO_6)_{0.7}$.

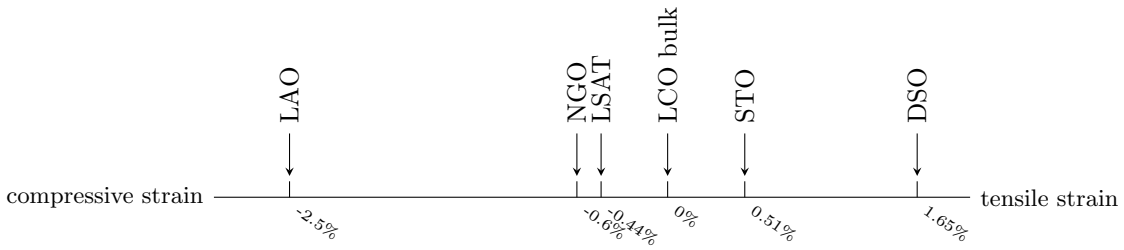

Figure 4.1: In-plane epitaxial misfit strain exerted by various substrates with respect to the pseudocubic lattice parameter of the bulk $LaCrO_3$.

4.2 Thin film characterization

We have grown the LCO thin films on five different perovskite substrates imposing both compressive and tensile strain. The relevant properties: their crystal structure, orientation, lattice parameters as well as pseudocubic lattice parameter, are listed in **table 4.1**. The in-plane misfit strains are depicted in **figure 4.1** and calculated according to **equation 3.1**. The expected c-value for known in-plane strain $\epsilon_{\parallel}$ and Poisson ratio ν, is calculated as follows

$$c_{\text{expected}} = c_{\text{bulk}} - \frac{2\nu}{(\nu - 1)} \frac{\epsilon_{\parallel}}{100} c_{\text{bulk}} \tag{4.1}$$

which is compared to the measured values discussed shortly in **section 4.2.1**

4.2.1 Crystalline structural characterization

The X-ray diffraction spectrum is a core part of the growth optimization and it is done after each sample growth. The $\vartheta/2\vartheta$-scans exhibit well-defined finite size oscillations indicating well-ordered, crystalline films (see **fig. 4.2a**). The fringes' spacing is dependent on the number of reflecting planes. This information, as well as the c-axis determined from the thin film's peak position, can be extracted using a Matlab fitting program [41]. The LCO//DSO is ~ 14.7 nm, LCO//STO film is ~ 13.6 nm, LCO//LSAT is ~ 13.3 nm, LCO//NGO is ~ 12.5 nm and the LCO//LAO film is ~ 12.6 nm thick. The extracted c-axis values are compared to the expected values obtained by equation 4.1 from the considerations made in section 2.3 using the Poisson value of $\nu = 0.23$, which is found in literature [16, 22], the misfit strain $\epsilon_{\parallel}$ discussed above and the pseudocubic lattice parameter for LCO $a_{pc} = 3.885\,\text{Å}$. In **figure 4.2b** the measured c-axis (in blue) and the expected values (in red) are plotted as a function of in-plane misfit strain. The experimental values are consistently larger than the expected values. The reason for this shift is unclear. Distortion of the c-axis values due to oxygen vacancies is unlikely (see figure 4.4c). In **figure 4.3** the out-of-plane strain $\epsilon_{\perp}$ is plotted against the in-plane strain. By fitting a line through the measured values and extracting its slope we can find the Poisson ratio of $\nu = 0.23 \pm 0.09$, which is in agreement with the value taken from literature.

The $\vartheta/2\vartheta$ scan of the LCO//NGO sample displays attenuated oscillations. Its repeated growth in these conditions yields the same poor quality every time (also see section 4.2.2). It is worth mentioning, that the growth on NGO was better in quality at higher oxygen contents of 0.11 sccm.

SCO requires post-growth annealing due to the formation of oxygen vacancies during the growth. Thus, we compared $\vartheta/2\vartheta$ measurements for as-grown and annealed LCO//LAO samples, that underwent the same annealing procedure as would the LCO/SCO//LAO superlattice. **Figure 4.4c** displays both scans. They have been fitted using the simulation software, which confirms that the LCO c-axis remains unaffected by the post-growth treatment.

Wide range symmetric $\vartheta/2\vartheta$-scans are performed to check if there is an occurrence of another phase. As an example, we conducted a wide scan for a ~ 50 uc thick LCO//LAO sample seen in

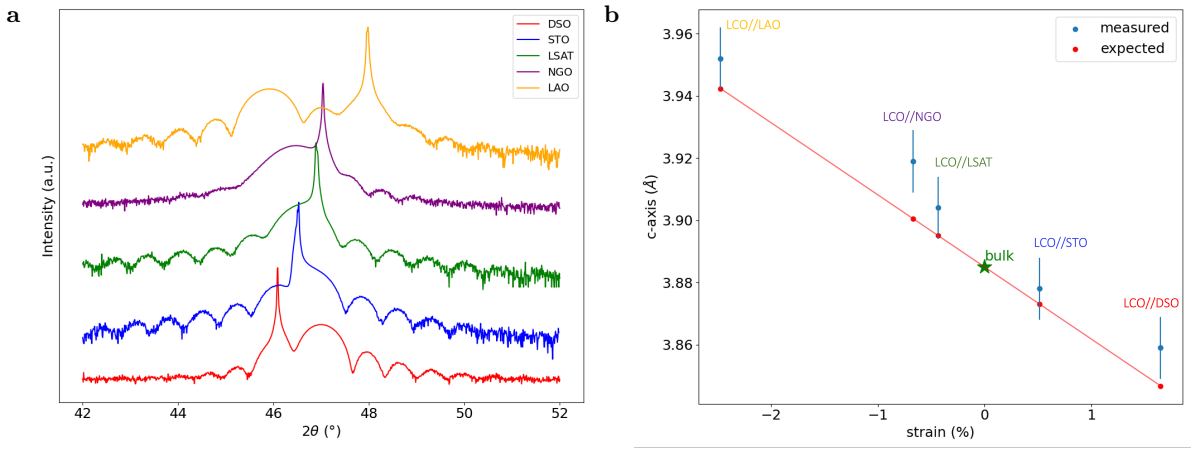

Figure 4.2: **(a)** XRD spectra of ~ 35 uc thick $LaCrO_3$ grown on different substrates as indicated. The c-axis peak of the film is the largest peak next to the substrate peak. DSO and STO exert tensile strain thus the film peak shifts to larger angles corresponding to smaller real space c-axis. LSAT, NGO and LAO have smaller in-plane lattice parameters than the LCO bulk leading to a compression of the unit cell resulting in a larger c-axis and thus film peaks at smaller angles with respect to the substrate peak. The clearly defined thickness fringes indicate a high degree of crystallinity with an atomically controlled interface and surface. **(b)** The c-axis extracted from the XRD spectra using the interactive fitting program [41] plotted as a function of strain. The red dots represent the expected c-axis considering the misfit strain and Poisson ratio found in the literature. The measured c-axis values lie systematically above the expected values.

figure 4.4a, which is the same sample presented in section 4.3. Only the (00l) LAO and LCO peaks are visible indicating a phase-pure epitaxial film. And in **figure 4.4b** the wide scan of the 35 uc LCO film on STO, also seen in **fig. 4.2a**, is shown also indicating a phase-pure film.

Figure 4.4d displays a reciprocal space map (RSM) for a 35 uc LCO//STO film around (103) substrate peak revealing a fully strained LCO//STO film. The map is displayed in the units 1/Å thus the conversion from reciprocal to real space is given by

$$d_{\text{real},x} = h \cdot \frac{1}{Q_x}$$

for the direction x in real space and h the miller index describing the peak (hkl). The position of the much fainter film peak was obtained by conducting a vertical cut through the two-dimensional map at the Q_x position of the substrate peak. The film's Q_x value is the same as that of the substrate meaning that the in-plane lattice parameter of the film is the same as the

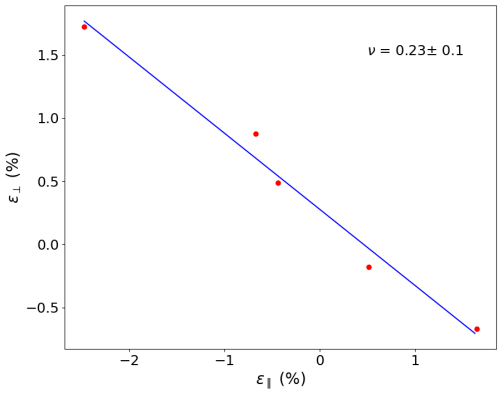

Figure 4.3: The out-of-plane strain, determined by the c-axis from XRD measurements, versus the nominal in-plane misfit strain. From the slope, the Poisson ratio, relating the two strains, is determined. The value obtained from the fit matches the Poisson ratio reported by literature $\nu = 0.23$.

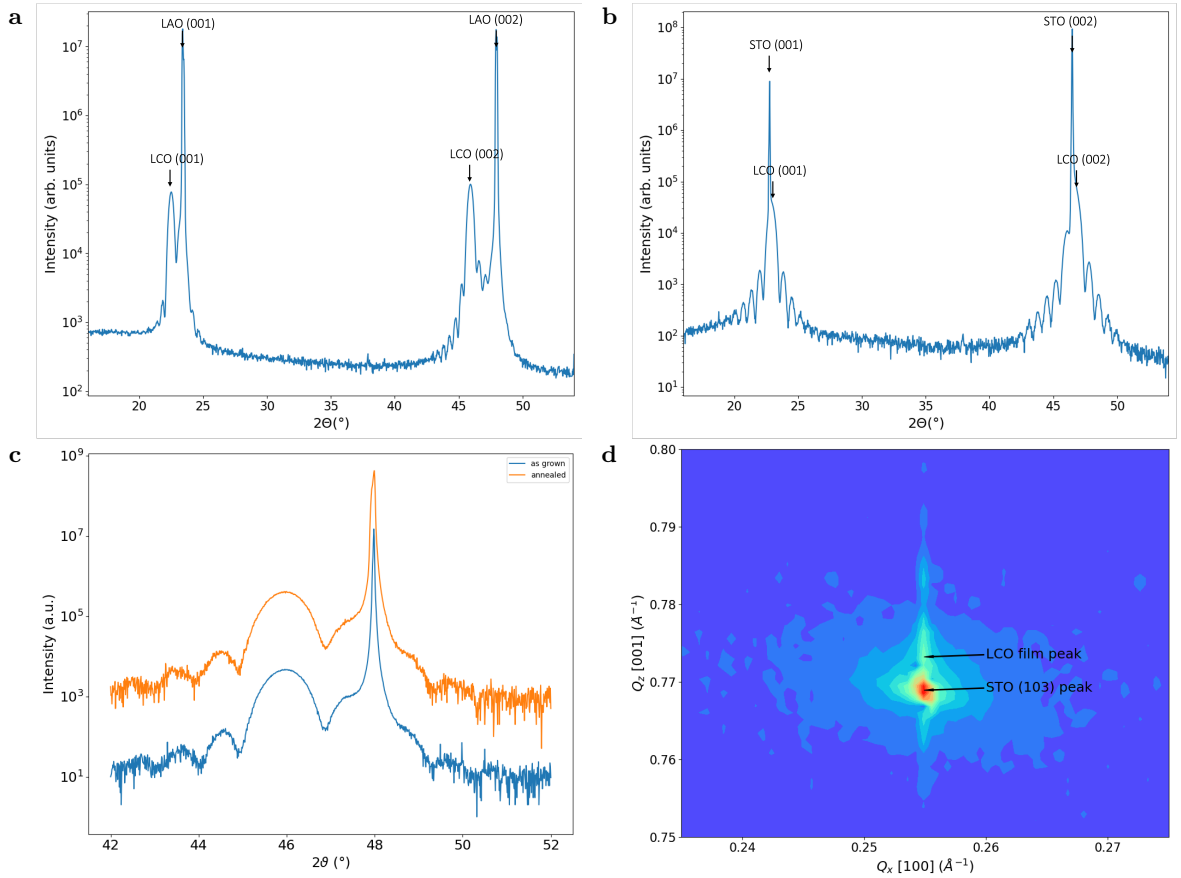

Figure 4.4: A wide $\vartheta/2\vartheta$ scan of a **(a)** LCO//LAO sample with 50 uc thickness and **(b)** LCO//STO with 35 uc thickness. Only the (001) and (002) peaks are visible confirming phase-pure films. **(c)** Symmetrical XRD scans at the (002) LCO and LAO peak comparing the as-grown (blue) and annealed (orange) LCO//LAO film. The comparison shows that annealing has no considerable effects on the LCO c-axis. **(d)** RSM of an LCO//STO sample confirming coherent epitaxial growth. We see the (103) Bragg peak of the (001)-oriented STO substrate accompanied by the fainter film peak very close to it as indicated in the image.

substrate confirming the film is coherently strained. In the vertical Q_z direction, the film peak is located at larger values than the substrate peak, as expected from the high-resolution XRD around the (002) substrate peak in **figure 4.2a**.

4.2.2 Surface morphology

The AFM images reveal the morphology of the film's surface. The images of the LCO films grown on different substrates were taken in non-contact mode. They are shown in **figure 4.5** and were processed as described in section 3.2.1. The images reveal smooth surfaces exhibiting the typical step and terrace structures indicating satisfactory layer-by-layer growth.

Line profiles were taken across the steps, indicated in each image, to determine the step height. A step height of 1 uc $\sim 4\,\text{Å}$ is expected and can be found for the films grown on DSO, LSAT, NGO and LAO. The LCO//STO sample exhibits a granular surface morphology due to an unterminated final layer. The step size is not identifiable.

The film surfaces reflect the reconstruction of the substrate's terrace structures. The terrace is determined by the substrate miscut. The miscut describes the angle at which the cut substrate deviates from the plane and plays a role in the way the surface atoms reconstruct themselves to minimize the surface energy influencing the width of the terraces. Comparing the scales of the different images with each other it becomes clear that the LSAT and the LAO substrates exhibit very wide terraces due to this low miscut, which the film follows.

The LCO//NGO appears to exhibit some form of uneven growth as there is the formation

of raised structures, on which the layers have grown nicely with 1 uc height. This is in line with the poorer crystalline quality observed in these films through XRD.

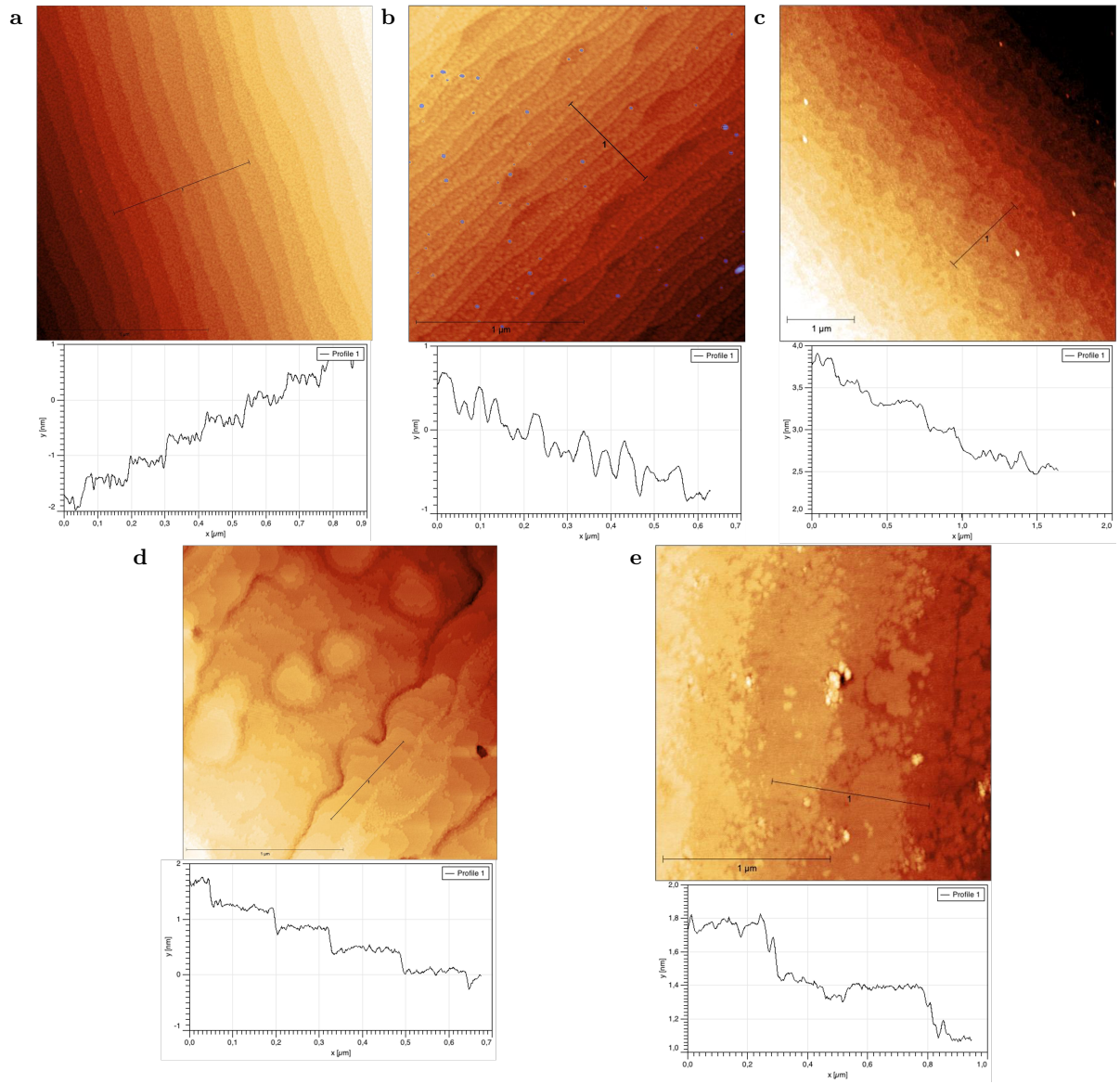

Figure 4.5: The AFM images of the strained LCO films and the respective line profile were used to determine the step sizes. **(a)** LCO on DSO, **(b)** LCO on STO, **(c)** LCO on LSAT, **(d)** LCO on NGO, **(e)** LCO on LAO.

4.2.3 Chromium Valence

The valence of Cr in the grown LCO films was investigated by x-ray absorption spectroscopy (XAS), which was conducted at PSI's Xtreme beamline in collaboration with Dr Cinthia Piemonteze.

XAS measurements were performed in total electron yield using circularly polarized light. The photon energy range were chosen to probe chrome's $L_{2,3}$ edge for transition from the $2p_{3/2}$ and $2p_{1/2}$ orbitals to the $3d$ orbital. The white line, or what is considered the XAS spectrum is given by $\mu = 1/2(\mu^+ + \mu^-)$, where the μ^+ and μ^- are the absorption coefficients of the right and left circularly polarized x-rays, respectively. The raw absorption intensity is normalized by the incoming photon flux. A linear background is fitted in the pre-edge energy region and subtracted from the data. The transitions into the continuum are approximated by an ad hoc double Fermi step function and also removed from the measured spectrum. The intensity spectra

of LCO//LAO, LCO//LSAT, and LCO//STO samples are shown in **figure 4.6**. The polarized spectra for each strain were normalized by the respective XAS intensity peak at the L_3 peak (at $\approx$ 576 eV). These spectra were measured in grazing incidence geometry with an applied field of 6 T for LCO//LAO and LCO//STO and of -6 T for LCO//LSAT. The XAS measurements can be directly compared to reference [22] confirming the Cr^{3+} valence state.

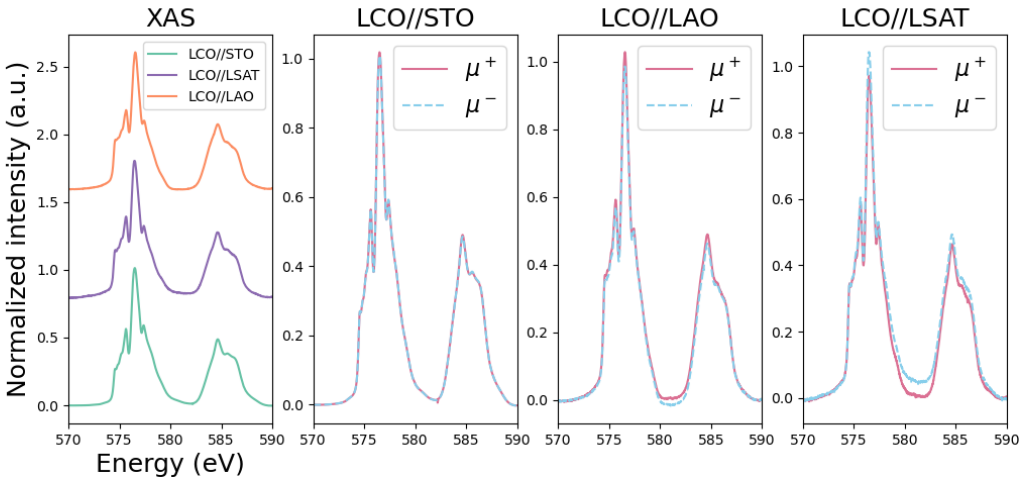

Figure 4.6: XAS intensity spectrum at the Cr L edge, μ^+ and μ^- for the LCO//STO, LCO//LAO, LCO//LSAT films which display typical Cr_3^+ (t_{2g}^3) multiplet structure according to reference [22].

XPS was conducted in-house at Prof. Thomas Greber's lab by Wei Chuang Lee. The XPS obtained by probing the Cr 2p orbital is shown in **figure 4.7a**. The energy of the detected electrons is analyzed and converted to the binding energy of the probed electrons by subtracting the kinetic energy from the photon energy which is $E_\gamma = 1253.6$ eV. This measurement was done for an LCO//STO sample sputtered with a higher O_2 flux of 0.01 sccm. The spectrum obtained is characteristic for Cr^{3+}. The existence of Cr^{4+} in the higher oxidation state of $LaCrO_4$ would lead to additional satellite peaks. Comparing with reference spectra from literature [42, 43] we can confirm that LCO maintains its Cr^{3+} valence state independent of the oxygen flux (see **fig. 4.7b**).

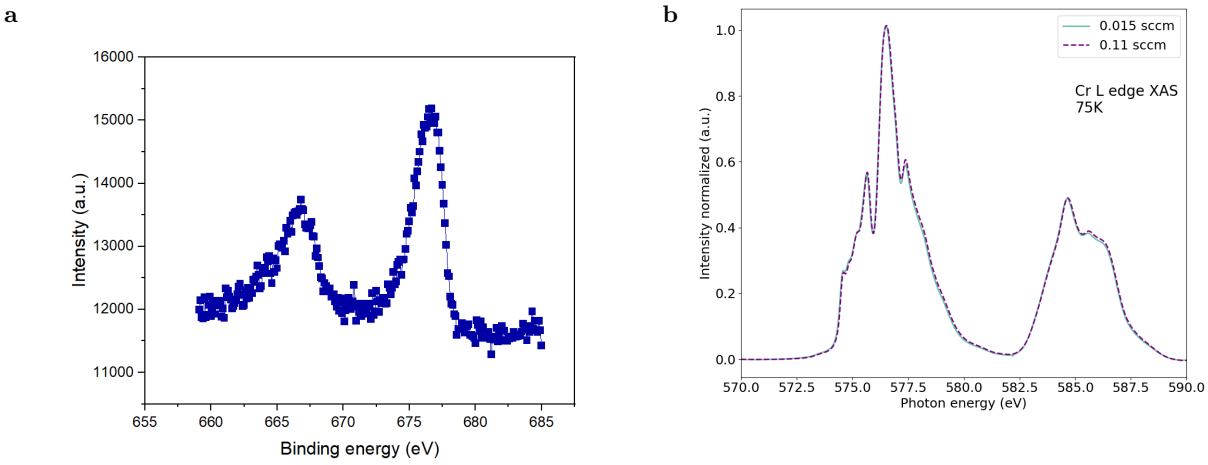

Figure 4.7: **(a)** XPS spectrum of a LCO//STO sample probing Cr 2p electrons. A characteristic spectrum for Cr^{3+}. **(b)** The normalized XAS intensity spectrum of the same sample confirms the Cr^{3+} oxidation state and compared to the LCO//STO sample shown in **fig. 4.6**, was grown at more oxidizing conditions.

4.2.4 Transport

We have conducted resistivity measurements for $LaCrO_3$ films using the method described in section 3.2.4. The contacts are made of platinum and were sputtered by dc-sputtering using a shadow mask. Here we present the transport property of LCO grown on STO (2.3 nm) and LAO (5.5 nm). LCO is insulating in bulk, which is the desired property for the LCO/SCO superlattice since we ultimately want to show that the antiferromagnetic spin ordering and the metallic character are coexistent. As shown in **figure 4.8** LCO//LAO shows clear insulating behaviour as the resistivity drastically increases with decreasing temperatures. However, when grown on $SrTiO_3$, the resistivity decreases with decreasing temperature indicating a metallic behaviour. It has already been reported that the LCO//STO interface becomes conducting due to the formation of a two-dimensional electron gas (2DEG) driven by a polar discontinuity [44, 45]. It should be noted that, when grown under low partial oxygen pressure the formation of oxygen vacancies is favoured, and this could also be a source of conductivity [46]. Therefore in **fig. 4.8** we also display the resistivity of the identical sample after annealing. STO has the following charged planes $(SrO)^0/(TiO_2)^0$ and the film $(LaO)^{+1}/(CrO_2)^{-1}$. Polar discontinuity arises at the interface of two layers where there is an abrupt change in the nominal charge of the planes leading to a built-up diverging potential, which is compensated by transfer or charge carriers to the interface leading to the 2DEG. What is especially interesting is the fact that both STO and LCO are insulating on their own. No drastic differences are visible for the LCO film on LAO. While LCO on STO still exhibits a metallic behaviour the resistivity altogether has increased. This behaviour is already known, annealing in O_2 atmosphere causes the sheet carrier concentration to saturate [46].

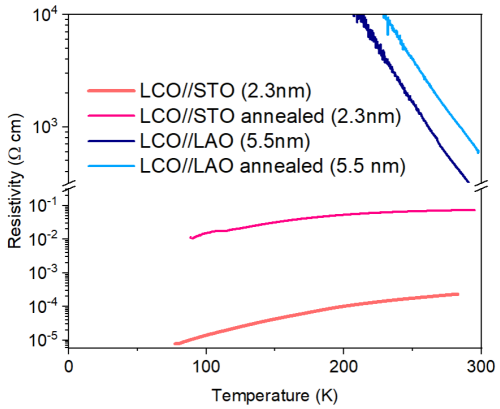

Figure 4.8: Resistivity versus temperature for highly conducting LCO//STO (red) and insulating LCO//LAO (blue) thin films.

4.3 Magnetism

We are interested now in studying the magnetic behaviour of LCO films as a function of strain. The magnetization measurements were done with the MPMS3 SQUID magnetometer by Quantum Design from the group of Prof. Dr Thomas Greber. The magnetic moment versus temperature and magnetic moment versus applied field measurements were done in VSM (vibrating sample magnetometer) mode for the in-plane and in the DC scan mode for out-of-plane geometry. In the standard approach to determine the magnetism of the films, the substrate itself is measured first and then, the exact same substrate is used to grow the desired thin film on top, which is then measured using the same measurement protocol. In this way, the substrate contribution can be removed from the total signal and we can study the film signal exclusively, as

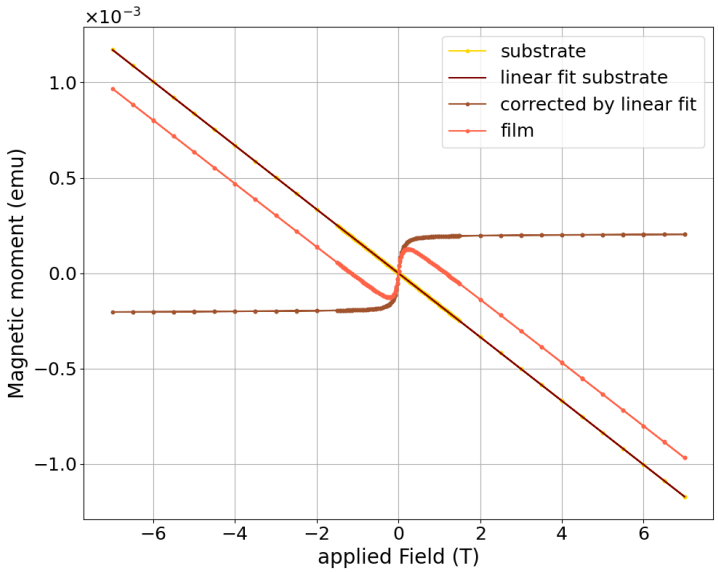

Figure 4.9: An example of magnetization versus magnetic field measurement at 200 K. The vertical axis is the magnetic moment in emu, which is the absolute magnetic moment measured by the SQUID and is the unit in which the data is presented. The yellow measurement is the substrate, which in this example is an LSAT substrate with an area of $5x5mm^2$. The orange curve corresponds to the raw film measurement, including the signal from the film and the substrate. The substrate contribution is purely diamagnetic at this temperature. By subtracting the substrate we are left with the brown curve, the film signal.

seen in **figure 4.9**. The LCO films studied in this section were grown on STO, LAO and LSAT, which contribute a diamagnetic background to the film measurement, i.e. a negative slope in the M(H) loops as seen in **fig 4.9**. At low temperatures, there is a paramagnetic contribution, as seen from the M(T) measurements in **figure 4.10**. This protocol is applied to all the M(T) measurements of the films, where the substrate signal is simply subtracted from the total signal. However, in the M(H) measurements of the films, the diamagnetic contribution is often removed by fitting the high field contributions by a line. This treatment was chosen because the subtraction of a sometimes noisy substrate signal can have a large impact on the comparatively small thin film signal, and to avoid potential unknown sources of differences between measurements such as sample pasting or misalignment.

We want to quantify the magnetic moment per unit cell or chromium atom. For that, we convert the units in which the measurement is taken (emu) into Bohr magnetons using the conversion factor

$$1\,\text{emu} = 1.0782822 \cdot 10^{20}\,\mu_B$$

Additionally, we estimate the total number of unit cells in the film in order to determine the magnetic moment per unit cell. For that, we need the in-plane lattice parameters a_{ip} of the substrate. The film is epitaxially grown on the substrate, so it will adapt the same in-plane lattice parameters. With that, we know the unit cell per area density $\rho = 1\,\text{uc}/a_{\text{ip}}^2$. From high-resolution X-ray diffraction measurements, we know the thickness of the film in number of unit cells N. The area of the film A which is the same as the substrate is known. The total number of unit cells in the film is given by

$$\#\,\text{uc} = \rho \cdot A \cdot N$$

By multiplying with the conversion factor and dividing by the total number of unit cells, we are left with the magnetic moment in Bohr magnetons per unit cell.

Furthermore, the moment is multiplied by a shape factor to compensate for misreported moments in VSM mode due to shape and size as reported by Quantum Design in reference [40]. The signal induced in the gradiometer is converted to an estimated magnetic dipole moment. This conversion is based on a cylindrical palladium standard sample, which is why for other geometries one needs to apply a shape factor.

Now, the films grown on different substrates can be compared with each other by extracting characteristic values to a ferromagnetic hysteresis curve like the remanence magnetization, the coercive field and saturation magnetization.

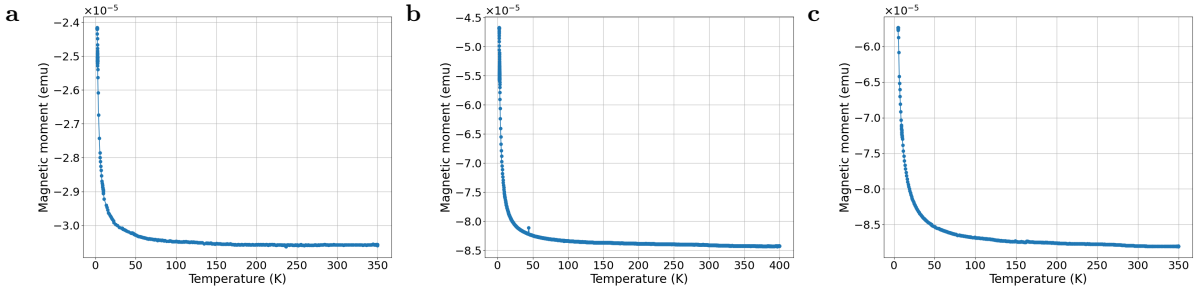

Figure 4.10: Magnetization M versus temperature T for the substrates **a)** STO, **b)** LSAT and **c)** LAO during field cooling at 0.5T.

4.3.1 Transition temperature

As mentioned in section 2.5, in LCO the weak ferromagnetic signal due to spin canting occurs below the antiferromagnetic Néel transition temperature, which in bulk LCO is $T_N \approx 290\,\mathrm{K}$ [16]. In order to determine the magnetic ordering transitions of the films we performed field-cooled (FC) magnetization versus temperature measurements from high temperatures (350 or 400K) to low temperatures (2-9K). The temperature range varies because of some difficulties with the respective instrument that restricted its use in the full temperature range. By subtracting the substrate measurement we get the film's signal. The transition temperature is then determined by taking the derivative of this corrected measurement and is defined by its peak position, i.e. the temperature at which the largest rate of change in the moment occurs. As shown in **figure 4.11**, for the 81 uc (32 nm) thick LCO on LSAT sample, we report a ferromagnetic transition at $\approx 290\,\mathrm{K}$ very close to the bulk Néel temperature. And for the 70 uc (27 nm) thick LCO on STO sample, the transition was found at $\approx 275\,\mathrm{K}$. In literature, the onset for a 36 nm LCO//LSAT and 39 nm LCO//STO film was reported to be $\approx 286\,\mathrm{K}$ [16]. The difference in thickness between those films and ours could account for the different transition temperatures. Indeed, we report the transition temperature $T_N \approx 268\,\mathrm{K}$ for an LCO//STO film corresponding to half the thickness of the film discussed above (35 uc, 14 nm) (see **fig. 4.11 c**). This transition temperature was determined by taking the derivative of the raw magnetic signal which was field cooled at 1 T. In the M(T) of the LCO//LAO sample, there was no transition visible, which is why it is omitted from this discussion. The nature of the signal at temperatures larger than the transition temperature in the thick samples (**fig. 4.11a 4.11b**) remains open.

Substrate	thickness (nm)	T_N (K)	thickness (nm)	T_N (K)
STO (001)	14/27	268/275	39	286 [16]
LSAT (001)	32	290	36	286 [16]
LAO (001)	-	-	-	-

Table 4.2: Transition temperature determined from our measurement (first column) and the comparison to literature values (second column)

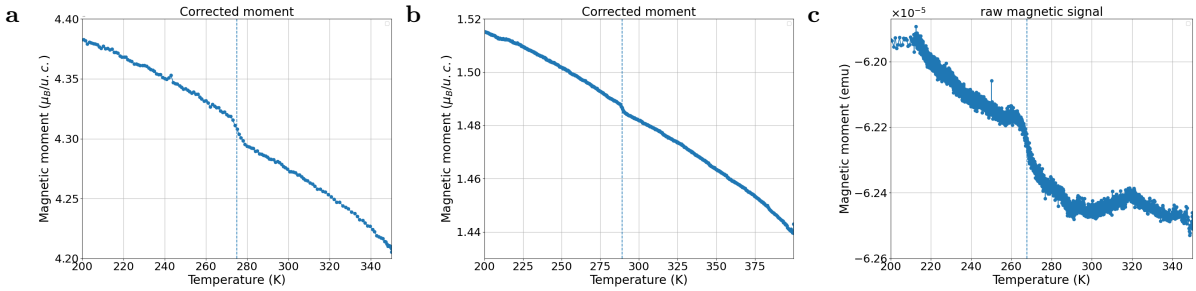

Figure 4.11: Field-cooled magnetic moment versus temperature curves. In **a)** LCO//STO of 70 uc thickness (FC +0.5T), **b)** LCO//LSAT of 81 uc thickness (FC +0.5T) and **c)** LCO//STO of 35 uc thickness (FC +1 T). The substrate contribution was removed by subtracting the previously done substrate measurement. The vertical lines indicate the determined transition temperatures.

4.3.2 M(H) loops

We conduct hysteresis measurements to study the material's strain-dependent *weakly* ferromagnetic properties. All samples were field-cooled with 0.5 T and magnetization versus applied field loops were measured at various temperatures. The as-measured M(H) loops at 10 K of the 20 nm thick LCO//LAO and the 27 nm thick LCO//STO film together with the substrate signal measurement before film deposition are shown in **figure 4.12**. From these measurements, we see that the ferromagnetic behaviour of the films is clearly discernible from the substrate contribution. Specifically, the magnetic signal of the LCO layer on the LAO film account for approximately 50%, while the LCO layer on STO film contributes approximately 15% of the total film-substrate contribution. This indicates that the signals from these samples are indeed quite strong. An example of an as-measured LCO on LSAT film at 200 K is shown in **figure 4.9**. The magnitude of the magnetic signal is larger than on STO and smaller than on LAO.

The M(H) loops of the LCO films strained by STO done at 10 K, 200 K, and 350 K, by LSAT done at 50 K, 200 K, and 300 K, and by LAO at temperatures 10 K, 200 K, and 300 K are shown in **figures 4.12c, 4.12d and 4.12e**. The total signal was processed by removing the linear fit of the substrate contribution at each specific temperature. The magnetic moments do not saturate in **figure 4.12e** and also in **4.12c** specifically at 200 K. The 10 K loop in **figure 4.12c** is an open loop, where the branches separate at high fields, probably due to a measurement artefact, as difficulties have arisen with the instrument at low temperatures. At 350 K, the slope at high fields vanishes for the LCO on STO case. In the M(H) loop of the LCO on LSAT film (**fig. 4.12d**), high-field contribution is much less distinct. In fact, in the LCO on LAO case, the magnetic moments even increase well above $3\,\mu_B$/Cr, which is the maximum spin contribution to the magnetic moment for three electrons not accounting for the normally much smaller orbital magnetic moment. Furthermore, the presence of a strong ferromagnetic signal even above the Néel temperature, i.e. at 300 K is puzzling and it is unclear if this is purely due to the film (see **fig. 4.11**).

The strength of the signal for canted spins and the saturation behaviour is striking. It is highly probable that the high-field contribution is due to a measurement artefact, some remaining substrate, or other contribution emerging during the film deposition or pasting process and requires further investigation. The measurements presented henceforth were corrected by a linear fit at the high-field regions correcting this slope. In **figure 4.13**, the hysteresis curves measured at 200 K of the strained LCO films are presented. The saturation values at 1 T are approximately $3.23, 1.57, 0.47\,\mu_B$/u.c. for the LCO films strained by LAO, LSAT (compressive), and STO (tensile), respectively. These results do not align with the smaller saturation values measured at 10 K for the LCO on STO and LSAT shown in the reference [16].

The remanence was extracted by interpolating the data points and determining the intersection with the vertical axis. The magnetization due to canting (the moment at 0 T) is ≈ 13 and 11 times smaller than the saturation for the LCO//LAO and LCO//LSAT samples, however

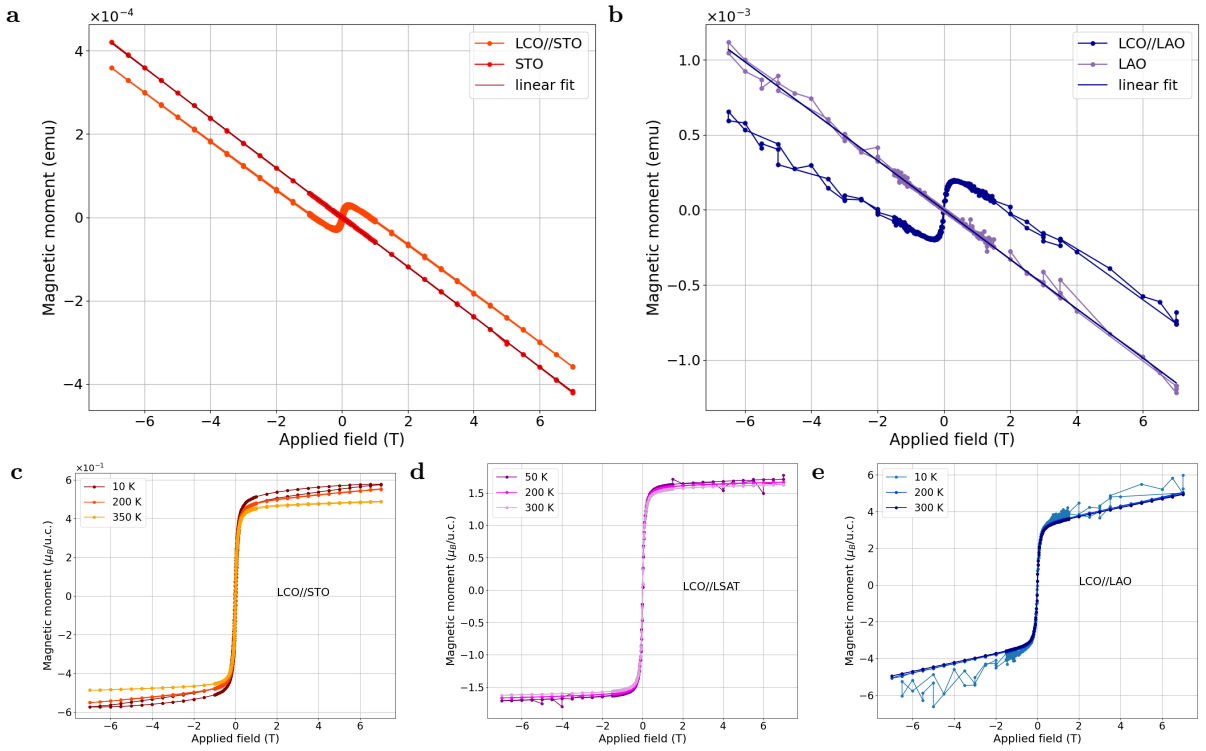

Figure 4.12: As-measured M(H) loop at 10 K for **(a)** LCO on STO and **(b)** LCO on LAO, including the respective separately measured substrate contribution and their linear fits. The processed M(H), where the linear fit to the substrate contribution is subtracted from the as-measured loops and converted to Bohr magnetons per unit cell: **(c)** the LCO on STO film at temperatures 10 K, 200 K and 350 K, **(d)** the LCO on LSAT film at temperatures 50 K, 200 K and 300 K and **(e)** the LCO on LAO film at temperatures 10 K, 200 K and 300 K. It is clear that the magnetic moments do not completely saturate and a remaining slope persists up to 300 K.

only ≈ 6 times smaller for the LCO//STO sample.

Figure 4.14a and **4.14b** show the comparison of the out-of-plane (oop) magnetization measurements with the in-plane (ip) measurements. The substrate contribution was removed by fitting a linear contribution to the high-field data in both the ip and oop measurements. They are in fact the exact same thin films measured in both geometries. Like this, the saturation magnetization for the oop at 2T is ≈ 1.54 and $0.28\,\mu_B$/uc for the LAO and STO strained LCO films respectively, well below the values obtained from the ip geometry. And so it appears, that the in-plane direction is the easy axis. Sharma et al report an experimentally observed easy-axis dependency on strain for LCO films grown on STO (ip easy axis) and LSAT (oop easy axis) backed by DFT calculations on the magnetic anisotropy energy (MAE) as a function of spin angles for 1% tensile and compressive strains. It should be noted that the DFT calculations show only a slightly larger MAE in the ip direction than the oop for the 1% compressive strain. Meaning, also in-plane orientations could be favoured. The calculations for nominal strain imposed by LAO are not available. Unfortunately, we are lacking oop data for the LCO//LSAT film. Our measurements do not follow the trend reported concerning the easy-axis but do follow the trend reported concerning the net magnetic moment dependency on the strain, i.e. increase with compressive strain. But again, as discussed throughout this subsection the measurements obtained demand further testing.

Since these results do not reproduce the measurements found in literature and because of the highly sensitive nature of these measurements, they need to be repeated as soon as the MPMS allows. A proposal for the continuation of this work will be given in the final chapter.

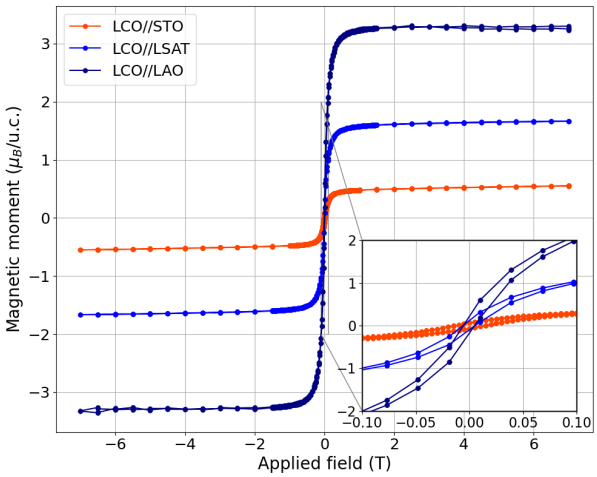

Figure 4.13: In-plane M(H) loops processed by subtracting the high-field linear slope in Bohr magnetons per unit cell of LCO on STO (red), on LSAT (blue) and on LAO (navy) at 200 K.

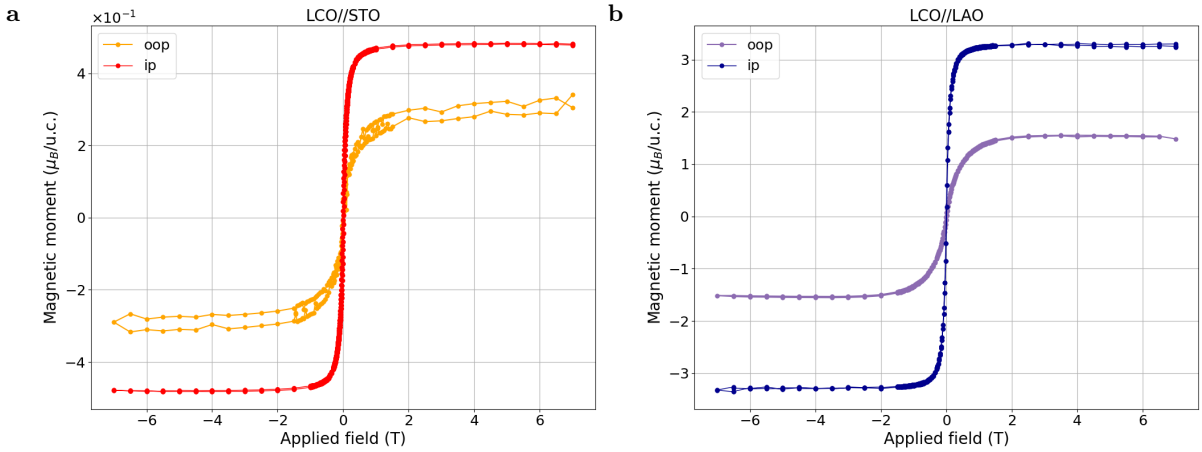

Figure 4.14: In-plane and out-of-plane measurement geometry for strained LCO films on **a)** STO and **b)** LAO at 200K.

4.3.3 X-ray Magnetic Circular Dichroism (XMCD)

To further investigate the magnetization of the films, we performed x-ray magnetic circular dichroism (XMCD) at the X-Treme beamline at the Swiss Light Source (SLS-PSI). An XMCD energy scan is obtained from the difference between the polarized energy scans performed at the absorption edge of interest

$$\text{XMCD} = \mu^+ - \mu^-$$

where μ^+ is the intensity measured with circularly positive (or right-handed) polarization and μ^- is the intensity measured with circularly negative (or left-handed) polarization. Please, refer to the appendix in Chapter 6 for more information on the measurement convention. The average is made from two to three scans per polarization. The individual polarized energy scans are processed as discussed in subsection 4.2.3 and normalized by the respective L_3 peak of the XAS. The XMCDs shown here are performed at the chromium L edge. The XMCD signal is proportional to the magnetic moment of the chromium ion. The quality of the signals does not allow for quantitative analysis, with which the spin and orbital magnetic moments could be determined, which is why the XMCDs are discussed qualitatively here.

For insulating thin films, like LCO on LAO and LSAT, charge accumulates on the surface creating electric fields that perturb the measurements. Charging can cause sample drifts, and

create background noise due to the interaction of the electric field with the x-rays resulting in additional signals and may affect the film's electronic properties itself. To counteract these effects as best as possible, we made sure each sample is properly mounted and grounded by contacting the sample's surface with silver paste as seen in **figure 4.15**.

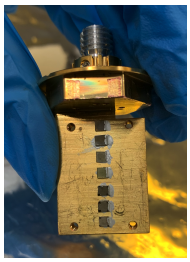

Figure 4.15: Image of the sample holder used during the Xtreme beamtime at SLS with the thin film samples pasted by silver paste.

The measurements presented in this subsection were done at 75K to further avoid charging effects. Despite these efforts, the difference between the highly insulating films and the conducting films is notable, as discussed below. There are two measurement geometries: *normal* refers to the 90° angle between the incident beam and the sample surface and *grazing* refers to the sample rotation of 60° away from the normal angle leading to a 30° incidence angle.

In **figure 4.16a**, the energy scans performed in grazing incidence of the 35 uc LCO film on STO, characterized by XRD in 4.2.1 and AFM in 4.2.2, are shown. The scans were taken at applied fields of -6 T, 0.5T, 2 T and 6 T. The XAS of this sample is shown in **figure 4.6**. It is clear that the XMCD signal at the resonance energy (576.5 eV) increases for larger field strength and reverses its sign with the sign of the field showcasing the magnetic moment of the chromium ions. To further study the ferromagnetic behaviour of this sample, we performed Cr hysteresis loops of the same sample also in grazing incidence, obtained from Cr XMCD signal by measuring at the on-resonance energy (the L_3 peak) and off-resonance energy at 570 eV respectively (indicated by stars in **fig. 4.16a** at each magnetic field. To get the asymmetry signal for each field sweep direction, the intensity measured with the right-handed circularly polarized (c+) light is subtracted by the intensity measured with left-handed polarization (c-). Following this procedure, however, led to a contradiction. The XMCD asymmetry does not have positive values for positive fields as was expected from the XMCD scans and the branch was multiplied by a factor of -1 in order for it to be consistent. The reason for this is not clear. In general, for such small XMCD signals the loops can be difficult, since they are based on just two pieces of information and cannot be monitored during the measurement. The results going from positive to negative fields are displayed in **figure 4.16b** confirming the saturation behaviour of the Chrome ions.

In **figure 4.17** the grazing incidence XMCD energy scans of LCO strained by STO (0.51%), LSAT (-0.44%) and LAO (-2.5%) are compared. The XMCD of the LSAT sample was acquired at -6 T, and therefore, it is multiplied by a factor of 1 in order to compare the signal with the other scans.

It is clear that the signal for the films grown on LAO and LSAT are noisier, especially in the region between the L_3 and L_2 range, the difference between the polarization curves leads to a comparatively large artefact instead of a baseline. The comparison of these rough scans indicates that the magnetic moment of the material increases with compressive strain as observed in the SQUID, although the relationship is not linear. The film grown on the substrate that applies a compressive strain of -0.44% (LSAT) seems to exhibit a larger magnetic moment than the film grown on the substrate that applies a more negative compressive strain of -2.5% (LAO). Both are larger than the magnetic moment observed under a tensile strain of 0.51%, which is in line with the SQUID measurements. Further statistics on these measurements would be required to confirm these preliminary results.

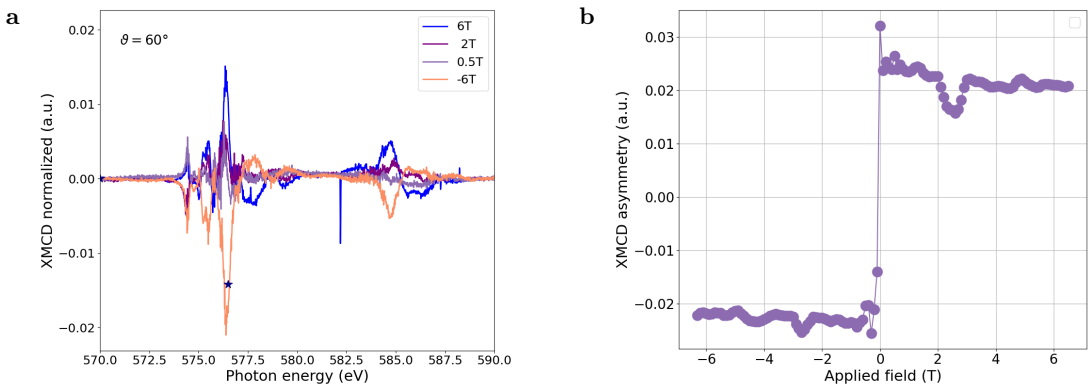

Figure 4.16: Grazing incidence XMCD energy scans of **(a)** LCO on STO for various fields and **(b)** the XMCD asymmetry versus field. The asymmetry is not normalized.

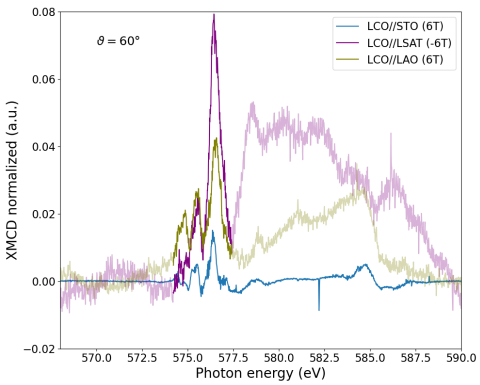

Figure 4.17: LCO on STO, LSAT and LAO at the magnitude of 6T. The scan done on LSAT at -6T was reversed for comparison. The noisier regions due to measurement artefacts are faint for clarity.

Figures 4.18 a)-d) display the XMCD scans taken under normal and grazing incidence per substrate. In **figure 4.18a**, the XMCDs of LCO on STO are shown. The difference between the two geometries is not very obvious in the L_3 region, and it is hard to make any statement on the easy magnetic axis, unlike the M(H) loops comparing ip and oop shown in subsection 4.3.2. However, both in **figure 4.18b** and **figure 4.18c** the XMCD signals point to an in-plane easy-axis for the LSAT and LAO films, like it was seen from the SQUID measurements on LAO. The magnetic moment seems to follow a similar trend in normal incidence as in grazing incidence. Namely, larger XMCD signals for compressively strained films than for tensile strain, as seen in **figure 4.18d**. It must be stated that the measurements done on LSAT and LAO are accompanied by noise and potential artefacts that lead to distortion, so the interpretation of these measurements is made within these limitations.

Figure 4.19 displays the magnetic properties of LCO films on STO grown under two different conditions: an O_2 flux of 0.11 sccm, and the one grown under a more reducing environment provided by a lower flux of 0.015 sccm. A larger XMCD signal is observed for the sample grown under larger oxygen pressure. These significant differences in this spectrum encourage the investigation of the magnetic properties of LCO grown with varying oxygen content to obtain a more complete understanding of the ferromagnetic behaviour. This is additionally backed by the fact that the films grown by Sharma et al in reference [16] are grown by PLD at an oxygen partial pressure of 0.026 mbar, which is a much more oxidizing environment compared to ours (order of 10^{-6} mbar).

Finally, we note that the films studied with XMCD are thinner (30-35 uc) than the ones studied by SQUID magnetometer (50-80 uc). For future studies, it would be valuable to investigate the relationship between the magnetic properties and the thickness of the films using a SQUID magnetometer, as this parameter could lead to the differences seen between the magnetic

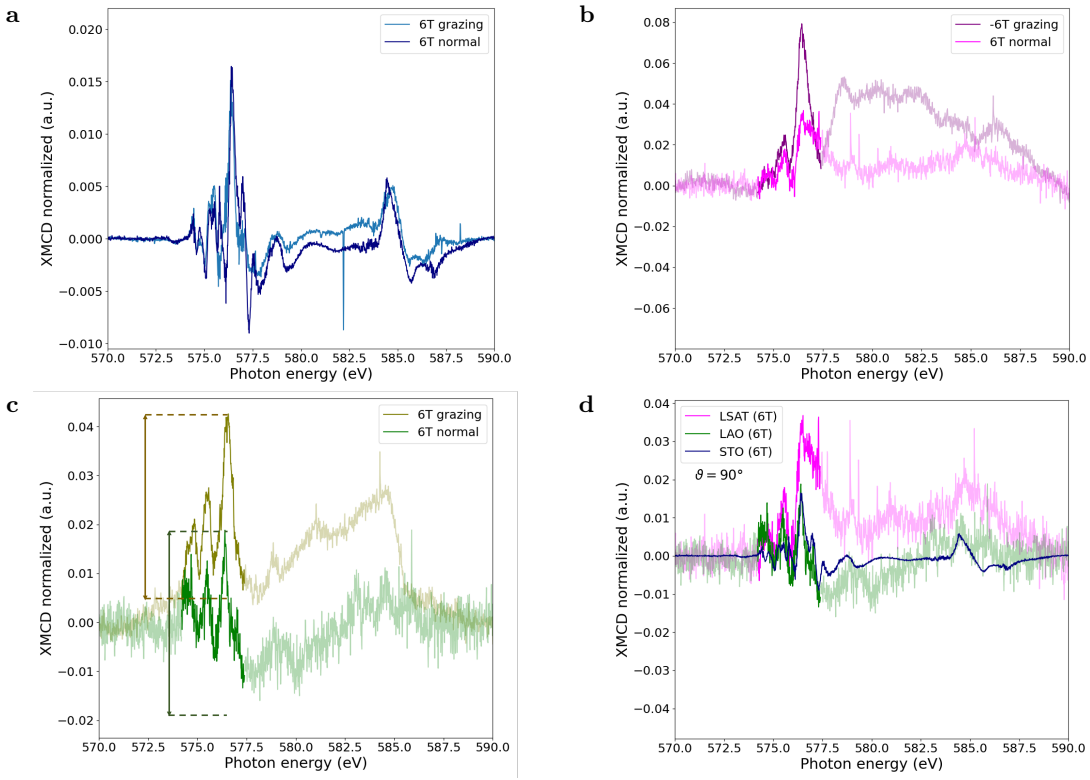

Figure 4.18: Comparison of normal (oop) and grazing incidence (nearly ip) XMCD energy scans at —6 T— grown on **(a)** STO, **(b)** LSAT and **(c)** LCO on LAO and **(d)** all. The noisier regions due to measurement artefacts are faint for clarity.

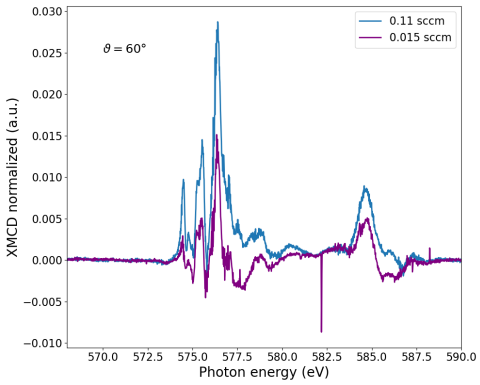

Figure 4.19: Cr XMCD signals in grazing incidence at 6T comparing LCO on STO thin films grown at 0.11 sccm and 0.015 sccm.

dichroism and SQUID measurements. Although XMCD signals can be used to study magnetic properties, the measurements obtained from LCO are very small approximately 1.5% of the XAS peak on STO, and therefore more susceptible to unreliable measurements due to drift or background noise. This can lead to significant distortions in the results, making it important to consider SQUID magnetometry for a more thorough investigation.

4.4 Preliminary characterization of superlattices

Some preliminary results on the LCO/SCO superlattices grown on LAO are compiled here. After optimization of the individual SCO and LCO layers, a growth rate calibration was conducted by performing three separate growths varying the sputtering time only for one layer leaving the other constant and vice versa. A growth rate of 9 s/uc was found for the LCO layer and

41 s/uc for the SCO layer. With this calibration, attempts were made at controlled growth of superlattices with (10,10)5, (5, 5)10, (18,18)3 where (# uc LCO, # uc SCO)x and x is the number of repetitions.

In **figure 4.20a** and **figure 4.20b**, the $\vartheta/2\vartheta$ measurements and the simulations best fitting the data are displayed. It is clear that the quality of the superlattices is not ideal since there are only some prominent peaks visible, and the finer structures are hidden by the broadening of the stronger peaks. This indicates that the interfaces between the alternating layers exhibit roughness, obstructing the interference of the reflecting X-rays. Nevertheless, the visible peaks were fitted using the expected thicknesses. It can be seen that the thicknesses of the repeating layers coincide ± 1 uc to what was aimed for using the growth rates from the calibration. The quality of the superlattices must be improved before performing magnetization measurements for the exchange bias since these measurements are very sensitive. As a first step, the growth rate of the LCO layer should be slowed down by reducing the rf power. This would achieve more control over the growth.

The AFM image in **figure 4.20c** of the (10,10)5 superlattice displays a smooth surface with some form of flaky layered morphology. The layers appear to be incomplete and not well-defined. The surface has not reconstructed the step and terrace structure of the substrate.

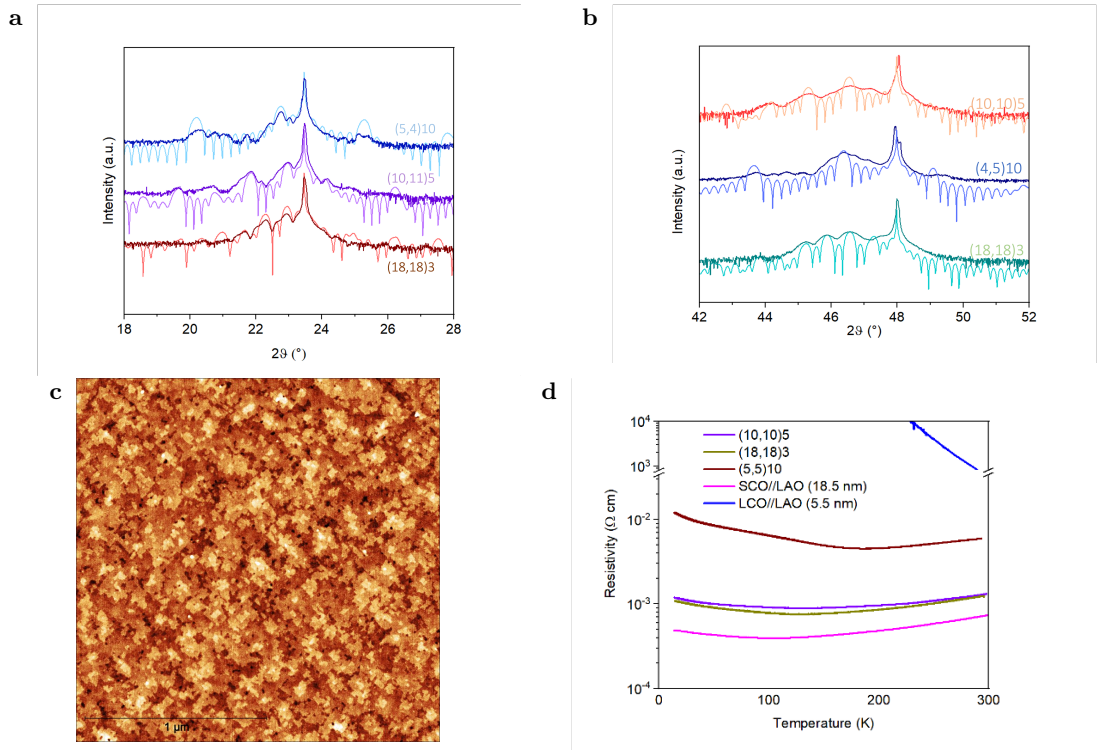

Figure 4.20: $\vartheta/2\vartheta$ scans around the **(a)** 001 and **(b)** 002 substrate and pseudocubic LCO peak of the three samples with the aimed for period: (10,10)5, (5, 5)10, (18,18)3. The respective simulations giving deviations of ± 1 uc are also shown. **(c)** AFM image of the (10,10)5 LCO/SCO//LAO superlattice. **(d)** Resistivity as a function of temperature for metallic SCO//LAO, superlattices with different bilayer thicknesses and insulating LCO//LAO. All samples have been annealed.

These superlattices were grown on LAO substrates to provide the strain required for the SCO to be metallic. It is in this state that we want to study SCO's magnetic properties. **Figure 4.20d** displays the resistivity of the superlattices together with a conducting annealed bare SCO//LAO film (~ 18.5 nm) and the insulating annealed LCO//LAO film previously shown in **figure 4.8**. SCO on LAO (pink) displays metallic transport properties and comparing all curves in the graph it is the lowest in resistivity. LCO//LAO (blue) is insulating, its resistivity increases drastically with decreasing temperatures. The superlattices' resistivity (brown, purple and olive) depends on the SCO layer's thickness. With increasing SCO thickness, the superlattices experience a

reduction in resistivity as the conducting layer's thickness is increased.

In **figure 4.21**, the M(H) measurement at 50 K after field cooling at 0.5 T is shown for the (10,10)5 LCO/SCO//LAO superlattice. No measurements under 50 K were possible due to instrument difficulties. It should be noted that in bulk the Néel transition temperature is actually at $\approx 40K$. However, muon spin relaxation measurements indicate a magnetic transition at $\approx 130K$. The magnetic moment was corrected by the substrate slope fit and was converted to Bohr magnetons using the total LCO thickness. By interpolating the data points with the x-axis the coercive fields $H_{c1} = 0.005 \pm 0.004$T and $H_{c2} = -0.006 \pm 0.004$ T are found. In the presence of exchange bias, we expect the coercive field from the two branches of the hysteresis to be asymmetric. The asymmetry reported here is not conclusive. As the error imposed by the instrument at low fields and the value for the coercive fields are of the same order of magnitude. The uncertainty comes from the low-field remanence of the MPMS magnet. By increasing the data point density at low fields and repeating the measurements one could make more qualified statements.

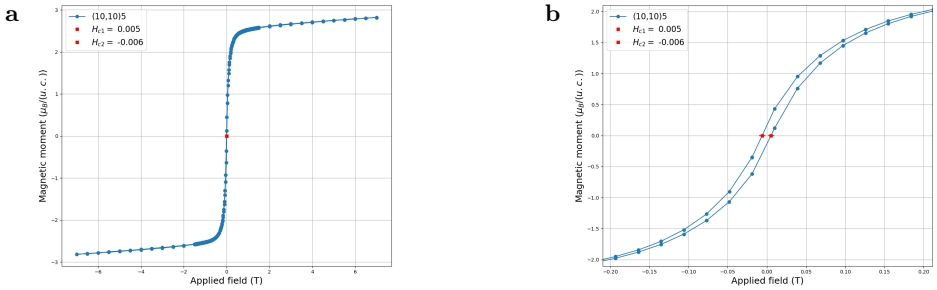

Figure 4.21: M(H) at $T = 50$ K of a (10,10)5 LCO/SCO//LAO superlattice and the coercive field determined by interpolating the data points with the horizontal axis $H_{c1} = 0.005 \pm 0.004$T and $H_{c2} = -0.006 \pm 0.004$ T.

Chapter 5

Conclusion & Outlook

In conclusion, we report the successful growth of LCO and promising first results concerning the growth of the LCO/SCO superlattices. The structural characterization of the LCO films demonstrates the high quality of the films, with the exception of the LCO grown on NGO that does not grow nicely at the 0.015 sccm O_2 flux conditions. The rapid growth rate of LCO leads to some uncertainty regarding the thickness for larger sputtering times. As seen in section 4.3, the thicknesses of LCO films on STO, LSAT and LAO for the same sputtering time vary quite a lot from each other. A clear first step is to reduce the LCO growth rate by decreasing the rf power during the sputtering process. Through that, more controlled growth can be achieved. The results on the magnetic properties discussed in subsection 4.3.2 are rather surprising and have not reproduced the measurements found in the literature. Particularly surprising is the ferromagnetic behaviour of films grown on LAO. Therefore, it would be quite valuable to conduct a comprehensive and systematic SQUID study for LCO thin films. For example, conducting measurements with sets of strained films with the same thickness to compare them with sets of other thicknesses to obtain a more complete characterization of the thickness and strain-related effects on the ferromagnetic properties. Additionally, it is important to consider the extremely reducing growth condition at which we fabricate our samples, which is necessary for the stabilization of the desired chrome valence in the SCO perovskite structure. This gas environment is much more reducing compared to the characterized films from literature, with which we compared our results regarding the magnetic properties. It would be very informative to be clear up to what extent these are condition-related effects. In conclusion, a more reliable understanding of the magnetic properties is needed for the ultimate goal of characterization of the magnetic properties of the LCO/SCO superlattice requiring a high degree of accuracy for the very small coercive fields. Reference [38] offers a comprehensive tutorial on conducting measurements on species with small coercive fields and magnetic moments.

While the preliminary results on the superlattice are promising, i.e. the transport properties are in line with our expectation, the growth rate was calibrated and the AFM image shows a promising layered but flaky morphology (no reconstruction of the substrate's surface), the interface roughness can be detrimental to the exchange bias effect. To further improve the chances of exchange bias the quality of the superlattices must be ameliorated. This will be done by reducing the LCO growth rate and starting with the optimization of bilayer systems, i.e. growth of an SCO layer on top of an LCO layer. The goal is to obtain more control over the growth since the layers need to be completed to obtain adequate interfaces. Thus, I would propose first the complete characterization of bilayer systems before moving on to superlattices and their magnetization measurements.

In summary, this work has laid down the important groundwork, which moving forward will inform further studies on LCO heterostructures.

Chapter 6

Appendix: XMCD Measurement Convention Clarification

In this appendix, I would like to give supplementary information on the measurement convention of XMCD. After completing this thesis, it was discovered that the magnet wiring at the Xtreme beamline deviates from the standard convention for calculating the XMCD signal. The magnetic field direction is wired in the opposite manner. To rectify this wiring issue, the XMCD signal is actually calculated using the formula:

$$\text{XMCD} = \mu^- - \mu^+$$

This implies that the data displayed in subsection 4.3.3 should be multiplied by -1. Importantly, this does not alter the interpretation of the XMCD scans as the overall signal remains the same. However, it should be noted that the issue concerning the XMCD loop remains as it arises by following the same convention.

List of Figures

Chapter 7

Bibliography

[1] The interface is still the device. *Nature Materials*, 11(2):91–91, 2 2012.

[2] Fabio Miletto Granozio, Gertjan Koster, and Guus Rijnders. Functional oxide interfaces. *MRS Bulletin*, 38(12):1017–1023, 12 2013.

[3] H. Y. Hwang, Y. Iwasa, M. Kawasaki, B. Keimer, N. Nagaosa, and Y. Tokura. Emergent phenomena at oxide interfaces. 11(2):103–113, 2012.

[4] Saima A. Siddiqui, Joseph Sklenar, Kisung Kang, Matthew J. Gilbert, André Schleife, Nadya Mason, and Axel Hoffmann. Metallic antiferromagnets, 7 2020.

[5] A Scholl, J Stöhr, J Lüning, J W Seo, J Fompeyrine, H Siegwart, J.-P Locquet, F Nolting, S Anders, E E Fullerton, M R Scheinfein, and H A Padmore. Observation of Antiferromagnetic Domains in Epitaxial Thin Films.

[6] Hans Lüth. *Solid Surfaces, Interfaces and Thin Films, Fifth Edition (Graduate Texts in Physics)*.

[7] Linlin Liu, Mingmei Jiang, Juanjuan Yin, Wenfeng Guo, and Tifeng Jiao. Preparation, sinterability, electrical transport and thermal expansion of Perovskite-type La0.8Ca0.2CrO3 composites. *Applied Sciences (Switzerland)*, 10(13), 7 2020.

[8] V.M. Goldschmidt. Die gesetze der krystallochemie. 14(21):477–485, 1926.

[9] Karin M. Rabe, Charles Ahn, and Jean-Marc Triscone. *Physics of ferroelectrics : a modern perspective*, volume 105. 2007.

[10] A M Glazer. Simple Ways of Determining Perovskite Structures. 31:756, 1975.

[11] Daniel Khomskii. *Transition metal compounds*.

[12] Anand Bhattacharya and Steven J. May. Magnetic oxide heterostructures. *Annual Review of Materials Research*, 44:65–90, 2014.

[13] Stephen Blundell. *Magnetism in Condensed Matter*. 2001.

[14] K. Momma and F. Izumi. Vesta 3 for three-dimensional visualization of crystal, volumetric and morphology data. *Journal of Applied Crystallography*, 44:1272–1276, 2011.

[15] Khuong P. Ong, Peter Blaha, and Ping Wu. Origin of the light green color and electronic ground state of $LaCrO_3$. *Physical Review B - Condensed Matter and Materials Physics*, 77(7), 2 2008.

[16] Yogesh Sharma, Binod Paudel, Jegon Lee, Woo Seok Choi, Zhenzhong Yang, Han Wang, Yingge Du, Kyeong Tae Kang, Ghanshyam Pilania, and Aiping Chen. Tuning magnetic and optical properties through strain in epitaxial LaCrO ¡sub¿3¡/sub¿ thin films. *Applied Physics Letters*, 119(7):071902, 8 2021.

[17] O. Polat, Z. Durmus, F. M. Coskun, M. Coskun, and A. Turut. Engineering the band gap of $LaCrO_3$ doping with transition metals (Co, Pd, and Ir). *Journal of Materials Science*, 53(5):3544–3556, 3 2018.

[18] Peter V. Sushko, Liang Qiao, Mark Bowden, Tamas Varga, Gregory J. Exarhos, Frank K. Urban, David Barton, and Scott A. Chambers. Multiband optical absorption controlled by lattice strain in thin-film LaCrO3. *Physical Review Letters*, 110(7), 2 2013.

[19] Khuong P. Ong, Ping Wu, Li Liu, and San Ping Jiang. Optimization of electrical conductivity of LaCrO3 through doping: A combined study of molecular modeling and experiment. *Applied Physics Letters*, 90(4), 2007.

[20] K. H.L. Zhang, Y. Du, P. V. Sushko, M. E. Bowden, V. Shutthanandan, S. Sallis, L. F.J. Piper, and S. A. Chambers. Hole-induced insulator-to-metal transition in L a1-x S rxCr O3 epitaxial films. *Physical Review B - Condensed Matter and Materials Physics*, 91(15), 4 2015.

[21] Alberto Carta and Claude Ederer. Evidence for Jahn-Teller-driven metal-insulator transition in strained SrCrO3 from first principles calculations. 4 2022.

[22] Junho Park, Dong Hwan Kim, Doopyo Lee, Kyung Tae Ko, Jong Hyun Song, Jae Young Kim, Tae Yeong Koo, Seung Ran Lee, and Jae Hoon Park. Thickness driven spin reorientation transition of epitaxial LaCrO3 films. *Applied Physics Letters*, 112(11), 3 2018.

[23] A. C. Komarek, T. Möller, M. Isobe, Y. Drees, H. Ulbrich, M. Azuma, M. T. Fernández-Díaz, A. Senyshyn, M. Hoelzel, G. André, Y. Ueda, M. Grüninger, and M. Braden. Magnetic order, transport and infrared optical properties in the $ACrO_3$ system (A = Ca, Sr, and Pb). *Physical Review B - Condensed Matter and Materials Physics*, 84(12), 9 2011.

[24] Zhi Li Zhu, Jin Hua Gu, Yu Jia, and Xing Hu. A comparative study of electronic structure and magnetic properties of $SrCrO_3$ and $SrMoO_3$. *Physica B: Condensed Matter*, 407(12):1990–1994, 6 2012.

[25] Luis Ortega-San-Martin, Anthony J. Williams, Jennifer Rodgers, J. Paul Attfield, Gunter Heymann, and Hubert Huppertz. Microstrain sensitivity of orbital and electronic phase separation in $SrCrO_3$. *Physical Review Letters*, 99(25), 12 2007.

[26] Giulia Bertino, Hsiang-Chun Hsing, Anna Gura, Xinzhong Chen, Theodore Sauyet, Mengkun Liu, Chang-Yong Nam, and Matthew Dawber. Strain control of the metal-insulator transition in epitaxial SrCrO thin films. 4 2021.

[27] L. W. Martin, Y. H. Chu, and R. Ramesh. Advances in the growth and characterization of magnetic, ferroelectric, and multiferroic oxide thin films, 5 2010.

[28] P J Kelly and R D Arnell. Magnetron sputtering: a review of recent developments and applications. Technical report.

[29] T. I. Selinder, G. Larsson, U. Helmersson, P. Olsson, J. E. Sundgren, and S. Rudner. Target presputtering effects on stoichiometry and deposition rate of Y-Ba-Cu-O thin films grown by dc magnetron sputtering. *Applied Physics Letters*, 52(22):1907–1909, 1988.

[30] F. Gunkel, D. V. Christensen, Y. Z. Chen, and N. Pryds. Oxygen vacancies: The (in)visible friend of oxide electronics. 116(12), 3 2020.

[31] J.M. Phillips. Substrate selection for thin-film growth. *MRS Bulletin*, 35–39(20), 1995.

[32] Peter Jonathan. Eaton and Paul. West. *Atomic force microscopy*. Oxford University Press, 2010.

[33] Contact mode. `https://www.parksystems.com/index.php/park-spm-modes/standard-imaging-mode/223-basic-contact-afm-dynamic-force-microscope-dfm`. Accessed: 2023-05-2.

[34] Ohler B. Donna H. Improved surface characterization with afm imaging. `https://www.techbriefs.com/component/content/article/tb/supplements/pit/features/applications/27833`, 2019. Accessed: 2023-05-2.

[35] George F. Harrington and José Santiso. Back-to-Basics tutorial: X-ray diffraction of thin films. *Journal of Electroceramics*, 47(4):141–163, 12 2021.

[36] Takeshi Osakabe. Principles and applications of multilayer mirror optics for X-ray diffraction measurements-CBO series for SmartLab. Technical report, 2017.

[37] R. L. Fagaly. Superconducting quantum interference device instruments and applications. 77(10), 2006.

[38] M. Buchner, K. Höfler, B. Henne, V. Ney, and A. Ney. Tutorial: Basic principles, limits of detection, and pitfalls of highly sensitive SQUID magnetometry for nanomagnetism and spintronics. *Journal of Applied Physics*, 124(16), 10 2018.

[39] Quantum Design. *Accuracy of reported sample moment: using the sample geometry simulator*, 8 2021. Rev. B0.

[40] Quantum Design. Accuracy of the Reported Moment: Sample Shape Effects. Technical report, 2010.

[41] Céline Lichtensteiger. InteractiveXRDfit: A new tool to simulate and fit X-ray diffractograms of oxide thin films and heterostructures. *Journal of Applied Crystallography*, 51(6):1745–1751, 12 2018.

[42] L. Qiao, T. C. Droubay, M. E. Bowden, V. Shutthanandan, T. C. Kaspar, and S. A. Chambers. LaCrO 3 heteroepitaxy on SrTiO 3(001) by molecular beam epitaxy. *Applied Physics Letters*, 99(6), 8 2011.

[43] X-Ray Photoelectron, Spectroscopy Tetraoxide, Hidetaka Konno, Hiroto Tachikawa, Atsushi Furusaki, and Ryusaburo Furuichi. Characterization of Lanthanum(III) Chromium(V). Technical report, 1992.

[44] Athby Al-Tawhid, Jordan R. Frick, Daniel B. Dougherty, and Divine P. Kumah. Growth-temperature dependence of conductivity at the $LaCrO_3$ /$SrTiO_3$ (001) interface . *Journal of Vacuum Science & Technology A*, 37(2):021102, 3 2019.

[45] Athby H. Al-Tawhid, Divine P. Kumah, and Kaveh Ahadi. Two-dimensional electron systems and interfacial coupling in $LaCrO_3$/$KTaO_3$ heterostructures. *Applied Physics Letters*, 118(19), 5 2021.

[46] Athby Al-Tawhid, Jordan R. Frick, Daniel B. Dougherty, and Divine P. Kumah. Growth-temperature dependence of conductivity at the $LaCrO_3$ /$SrTiO_3$ (001) interface . *Journal of Vacuum Science & Technology A*, 37(2):021102, 3 2019.